

PORE PRESSURE AND FLUID FLOW BENEATH THE FRONTAL THRUST OF THE  
KUMANO BASIN TRANSECT, JAPAN: INFLUENCE ON DÉCOLLEMENT  
PROPAGATION

By

KATHERINE ROWE

A THESIS PRESENTED TO THE GRADUATE SCHOOL  
OF THE UNIVERSITY OF FLORIDA IN PARTIAL FULFILLMENT  
OF THE REQUIREMENTS FOR THE DEGREE OF  
MASTERS OF SCIENCE

UNIVERSITY OF FLORIDA

2011

© 2011 Katherine Rowe

To my brothers, who encouraged me to pursue a career in science and to my mother,  
who has supported and encouraged me through my education

## ACKNOWLEDGMENTS

First and foremost, I would like to thank my adviser, Dr. Elizabeth Screaton, for her unwavering patience, help, and support in learning Abaqus and writing this thesis. I would not have been able to do this without her guidance for two and a half years. I would also like to thank Dr. John Jaeger and Dr. Jon Martin, for their comments and encouragement through this process. Additionally, I would like to thank Dr. Andre Hüpers for sharing his data to help the thesis come together. This research used samples and data provided by the Integrated Ocean Drilling Program (IODP). Funding for this research was provided by the Consortium of Ocean Leadership U.S. Scientist Support Program post-cruise grant to Screaton and National Science Foundation grants OCE-0623358, OCE-0727023 and OCE-0751497. I want to thank the Department of Geological Sciences for the learning experiences and great times. For edits and comments, I would like to thank Pati Spellman. I would like to thank Stephen Rowe for being supportive and listening about my modeling issues. For encouragement, I would like to thank Annette Farah. Lastly, I would like to thank Alex Hastings for the encouragement, multiple proof reads, edits, and peanut butter and jelly sandwiches.

## TABLE OF CONTENTS

	<u>page</u>
ACKNOWLEDGMENTS.....	4
LIST OF TABLES.....	7
LIST OF FIGURES.....	8
LIST OF ABBREVIATIONS.....	9
ABSTRACT.....	11
CHAPTER	
1 INTRODUCTION.....	13
2 GEOLOGICAL BACKGROUND.....	16
Nankai Trough.....	16
Kumano Basin Transect.....	17
3 EQUATIONS OF FLUID FLOW AND DEFORMATION.....	29
Fluid Flow.....	29
Elastic and Poroelastic Deformation.....	30
Plastic Deformation.....	33
Friction.....	34
4 PREVIOUS NANKAI INVESTIGATIONS.....	36
Previous Nankai Trough Modeling.....	38
Previous Fully Coupled Subduction Zone Fluid and Deformation Models.....	39
5 MODEL DESIGN.....	41
Modeling Approach.....	41
Modeling Setup.....	41
Modeling Procedure.....	42
Modeling Parameters.....	43
6 RESULTS.....	50
Permeability Results.....	50
Modeling Results.....	50
Base Model Results.....	51
Sensitivity Results.....	52

7	DISCUSSION .....	61
	Pore Pressure and Fluid Flow.....	61
	Décollement Propagation.....	63
8	CONCLUSIONS .....	65
	LIST OF REFERENCES .....	66
	BIOGRAPHICAL SKETCH.....	73

## LIST OF TABLES

<u>Table</u>		<u>page</u>
4-1	Log-linear permeability-porosity relationships of the Shikoku Basin clay.....	40
5-1	The parameters used within the base model simulations with references.....	47
6-1	Maximum simulated excess pore pressures (Pa), the calculated $\lambda^*$ , and the maximum fluid velocity (m/s). .....	54

## LIST OF FIGURES

<u>Figure</u>		<u>page</u>
2-1	A map depicting the Ashizuri, Muroto, and Kumano Basin transects .....	21
2-2	The seismic profile of the Kumano Basin transect.....	21
2-3	The frontal thrust region of the Kumano Basin transect.....	22
2-4	The stratigraphic profile of Site C0006 .....	23
2-5	The stratigraphic profile for Site C0007 .....	24
2-6	The stratigraphic profile for Site C0007 .....	25
2-7	The stratigraphic profile of Site C0011 .....	26
2-8	The stratigraphic profile of Site C0012 .....	27
2-9	The porosity-depth profiles from the incoming sediments of the Kumano Basin and Muroto transects.....	28
3-1	A representation of consolidation curve and the swelling curve .....	35
5-1	An illustration of the model setup.....	48
5-2	The temperature distribution used for viscosity calculations.....	49
6-1	The grain-size grouping of the permeability of Sites C0006 and C0007 samples plotted as a function of porosity.....	55
6-2	The Shikoku Basin facies permeability-porosity trends. ....	55
6-3	Simulated excess pore pressure through time. ....	56
6-4	The excess pore pressure results.....	57
6-5	Cumulative horizontal displacement simulated with the base model. ....	58
6-6	The fluid flow results.....	59
6-7	The excess pore pressure ratio results for the sensitivity analyses.....	60

## LIST OF ABBREVIATIONS

a	Compressibility ( $\text{ms}^2/\text{kg}$ )
B	Skempton's Coefficient (Unitless)
$C_c$	Compression Index (Unitless)
$C_s$	Swelling Index (Unitless)
$\gamma$	Slope (Unitless)
E	Young's Modulus (Pa)
e	Void Ratio (Unitless)
$\epsilon$	Strain (Unitless)
g	Gravity ( $\text{m/s}^2$ )
h	Head (m)
K	Hydraulic Conductivity (m/s)
k	Permeability ( $\text{m}^2$ )
$\kappa$	Log Bulk Modulus (Unitless)
$\Lambda$	Plastic Log Bulk Modulus (Unitless)
$\lambda^*$	Pore Pressure Ratio (Unitless)
$\mu$	Viscosity (kg/ms)
n	Porosity (Unitless)
$\nu$	Poisson's Ratio (Unitless)
P	Pore Pressure (Pa)
$\rho$	Density ( $\text{kg/m}^3$ )
$R_m$	Fluid Source Term ( $\text{kg/m}^3\text{s}$ )
S	Storage (1/m)
$\sigma$	Stress (Pa)

T	Temperature (°C)
t	Time (s)
V	Volume (m <sup>3</sup> )
v <sub>f</sub>	Fluid Velocity (m/s)
χ	Coefficient of Friction (Unitless)
z	Depth (m)

Abstract of Thesis Presented to the Graduate School  
of the University of Florida in Partial Fulfillment of the  
Requirements for the Masters of Science

PORE PRESSURE AND FLUID FLOW BENEATH THE FRONTAL THRUST OF THE  
KUMANO BASIN TRANSECT, JAPAN: INFLUENCE ON DÉCOLLEMENT  
PROPAGATION

By

Katherine Rowe

August 2011

Chair: Elizabeth Screaton  
Major: Geology

Results of a coupled fluid flow-deformation model illustrate the influence of excess pore pressure, friction, and stress on décollement propagation in the Kumano Basin transect offshore Japan. Numerical modeling suggests that displacement along the shallow frontal thrust generates excess pore pressure of approximately one third of the overburden. The maximum excess pore pressure is located ~0.6 km in depth below the frontal thrust and about 7 km landward of the trench. The fluid flow patterns within the simulation depict the fluid flowing horizontally through the permeable Lower Shikoku Basin sandstone and vertically through the permeable trench sediments. Modeling results suggest that two previously proposed mechanisms may both contribute to décollement propagation. At 7 km landward of the trench, a large excess pore pressure occurs with a minimum in the effective stress. This result is consistent with previous suggestions that the décollement propagates along a horizon with high pore pressure and low effective stress. In contrast, at the trench, a small excess pore pressure occurs beneath the trench, with no observable minimum in effective stress. Instead, comparison of horizontal and vertical effective stresses indicates that horizontal

compression is occurring seaward of the frontal thrust in the upper portion of the underthrust sediments, while vertical effective stress exceeds horizontal effective stress within the lower footwall sediments. This stress rotation is consistent with décollement propagation controlled by gradients in horizontal compaction, as has been proposed due to lateral compression transmitted across the frontal thrust.

## CHAPTER 1 INTRODUCTION

Sediment-rich subduction zones, such as the Nankai Margin offshore of the coast of Japan, experience repeated earthquakes of magnitude 8 or greater (Ruff and Kanamori, 1983). The Nankai Trough Seismogenic Zone Experiment (NanTroSEIZE) project is focused on understanding the mechanics and seismic activity within the Kumano Basin transect along the Nankai Margin. This project is actively studying the aseismic to seismic transition, earthquake and tsunami generation, and the hydrologic behavior of plate boundaries (Tobin and Kinoshita, 2006 a, b). The first stage of drilling as part of the Integrated Ocean Drilling Program (IODP) included examination of the frontal thrust at the toe of the accretionary prism, investigating its evolution, the relationship between deformation, fluid behavior, and slip, and its function in large earthquakes (Tobin and Kinoshita, 2006 a, b).

Understanding the hydraulic behavior of the system can allow insight into deformation. Pore pressure and permeability play an important role in deformation at subduction zones, and thus are an important component of NanTroSEIZE. Permeability influences the direction and rate of the fluid flow through the region. As a result, it controls the drainage of pore pressure and the increase in effective stress (Saffer and Bekins, 2002). Effective stress can affect fault strength, deformation, and structural development (Saffer, 2003), and can alter the shape of the accretionary complex (Saffer and Bekins, 2002). Characterizing the pore pressure buildup within fault zones can allow for better predictions of fault movement (Tobin and Saffer, 2009). In addition, pore pressures may also help to control the propagation of the décollement zone. The décollement zone is the structural and mechanical boundary between the accreted and

subducted sediments (Moore, 1989). At greater depths, this plate boundary becomes the seismogenic zone. The décollement is thought to originate along a layer of low strength, underconsolidation, and excess pore pressure (Moore, 1989). Le Pichon and Henry (1992) suggest that the formation of the protodécollement occurs in the level of least mechanical resistance, which is believed to contain high pore pressures. In contrast, Raimbourg et al. (2011) argue that the thrusting of the prism creates horizontal compression seaward of the frontal thrust, which controls the propagation of the décollement.

Prior to NanTroSEIZE, Nankai margin drilling focused on two transects, Muroto and Ashizuri, located to the west of the Kumano Basin transect. The Muroto transect is unique in that it has high heat flow, with basement temperature exceeding 100°C seaward of the deformation front (Moore et al., 2001; Moore et al., 2009; Saffer, 2010). In contrast, the Ashizuri and Kumano Basin transects are considerably cooler. The Kumano Basin frontal thrust exhibits a shallow dip angle ( $<10^\circ$ ) and has been thrust over ~6 km seaward on top of the trench sediments. In contrast, the Muroto and Ashizuri frontal thrusts of the Nankai prism have steeper dip angles (~25-30°) and are only displaced by ~1-2 km (Moore et al., 2009). While all three transects contain sandy trench sediment, both the Ashizuri and Kumano Basin transect have buried sandy turbidites while the Muroto transect does not. Underwood et al. (2009) suggested underthrust turbidites may enhance dewatering and focus fluid flow from depth. Recent drilling results suggest that the buried sand layer may allow geochemical signals of flow from depth to reach 20 km seaward of the deformation front (Underwood et al., 2009).

Previous modeling investigations have allowed for better understanding of the hydrological behavior and formation of the décollement, including identifying variables that influence hydraulic behavior, estimating excess pore pressure, and examining hydrological influence on fault strength (Saffer, 2010; Skarbek and Saffer, 2009; Gamage and Screaton, 2006; Screaton et al., 2002). The majority of investigations have been focused on the Muroto transect due to more information available there (Skarbek and Saffer, 2009; Gamage and Screaton, 2006). One exception is a study by Saffer (2010) who compared the lithological influence on pore pressure and prism shape of the Ashizuri and Muroto transects. Saffer (2010) found that buried sandy turbidites in the Ashizuri transect resulted in lower excess pore pressures than the Muroto transect.

Although previous hydrogeological models of Muroto and Ashizuri transects have helped to assess pore pressures and effective stress conditions there, differences in geometry, heat flow, and lithology complicate the transfer of results to the Kumano Basin transect. In this paper, results of laboratory tests of permeability are integrated into a finite-element model of plastic deformation and fluid flow in the Kumano Basin transect. Modeling is a key tool for investigating the depths below that reached by drilling. First, the modeling examines whether deformation occurs rapidly enough relative to fluid escape to generate significant excess pore pressures, as have been inferred for the Muroto and Ashizuri transects, or whether the buried sand layers result in rapid dewatering. Second, the modeling will help to understand the relationship between fluid pressure, deformation, and the propagation of the décollement zone. The use of a fully-coupled deformation and fluid flow model allows assessment of both hydrologic and mechanical conditions that might influence décollement propagation.

## CHAPTER 2 GEOLOGICAL BACKGROUND

### **Nankai Trough**

The Nankai Margin is one of the most studied subduction zones with earthquake and tsunami records going back over 1300 years (Ando, 1975). The Nankai Trough is formed by the subduction of the Philippines Sea Plate beneath the Eurasian Plate at 40–65 km per million years (Seno et al., 1993; Miyazaki and Heki, 2001). Prior to NanTroSEIZE, drilling and other investigations along the Ashizuri and Muroto transects have helped to characterize the Nankai Margin (Figure 2-1). The Shikoku Basin facies is deposited on the incoming plate, and trench sediments are deposited near the deformation front. The predominantly hemipelagic mud of the Shikoku Basin is separated into the Upper Shikoku Basin and the Lower Shikoku Basin facies. The boundary between the lower and upper Shikoku Basin facies is a diagenetic transition that is related to breakdown of opal cements (Spinelli et al., 2007). Another distinction between the upper and lower Shikoku Basin (LSB) facies is the occurrence of sandy turbidites within the LSB (Moore et al., 2001). The LSB sandstones are generally deposited in basement lows and absent from basement highs (Ike et al., 2008).

There are notable topographical, thermal, and mechanical differences between the Muroto and Ashizuri transects. The Muroto transect is located on top of a topographic high, which prevented the deposition of the LSB sandstones that are seen in the Ashizuri transect. Due to the Muroto transect being located near an extensional ridge that ceased spreading 15 Ma, it contains a higher heat flow and observed temperatures than the Ashizuri transect (Moore et al., 2001). In addition, a rapid accretionary outgrowth of 20km/my during the past 2 My is observed in the slope of the Muroto. The

rapid growth is suggested to be caused by a seamount that was subducted ~2 Ma, creating a large embayment. The rapid growth reflects the prism rapidly trying to recover the frontal accretion across over the embayment area (Moore et al., 2001). Such rapid growth is not observed in the Ashizuri transect.

In both transects, the décollement zone near the deformation front is localized in the Lower Shikoku Basin facies, within sediments with ages of ~5.9–7.0 Ma (Moore et al., 2001). This lies above the LSB sandstones of the Ashizuri transect. The proto-décollement, the extension of the décollement beneath the frontal thrust, has been estimated to correlate to a depth of ~400mbsf in the incoming sediments (prior to deposition of trench deposits) of the Lower Shikoku Basin facies, in both the Muroto and Ashizuri transects (Shipboard Scientific Party, 2000; Shipboard Scientific Party, 2001; Moore et al., 2005).

### **Kumano Basin Transect**

The frontal thrust and incoming sediments of the Kumano Basin transect offshore the Kii Peninsula, Japan, were drilled during IODP Expeditions 314 and 316 in 2007-2008 and Expedition 322 in 2009 (Figures 2-1 and 2-2). In this transect, the frontal thrust of the accretionary prism has moved the prism more than 6 km seaward on top of the trench sediments at a shallow dip angle, <10° (Moore et al., 2009). In contrast, the Muroto and Ashizuri frontal thrusts of the Nankai prism have steeper dip angles (~25-30°) and are only displaced by ~1–2 km. This unusual geometry of the Kumano Basin transect suggests that normal frontal imbrication was interrupted, perhaps due to a variation in incoming basement structure, sediment thickness, or lithology (Moore et al., 2009). Development of a protothrust zone (PTZ) seaward of the frontal thrust indicates that frontal imbrication may be resuming (Moore et al., 2009) (Figure 2-3). Screamon et

al. (2009) used seismic reflection profiles and data derived from IODP Expedition 316 cores to estimate that the earliest initiation of the frontal thrust fault occurred about 0.78 Ma-0.436 Ma.

During IODP Expedition 316, Sites C0006 and C0007 were drilled to examine the main frontal thrust region located at the toe of the accretionary prism, and to investigate the relationship between slip, deformation, and fluid flow (Screaton et al., 2009) (Figures 2-2 and 2-3). Drilling during Expedition 316 reached ~603 mbsf for Site C0006 and ~484 mbsf for C0007 (Expedition 316 Scientist, 2009a and b). Greater depths ~885 m below seafloor, were reached at Site C0006 during Expedition 314, in which logging-while-drilling was conducted but no cores were collected (Expedition 314 Scientists, 2009). Temperatures in the drilled section are predicted to be <40°C with a 27°C/km gradient at Site C0006 and a 42°C/km gradient at Site C0007, based on extrapolation of borehole temperature measurements (Figure 2-2). Using nanofossils the ages from Sites C0006 and C0007 ranged from less than 1 Ma near the surface to greater than 5 Ma with depth (Expedition 316 Scientists, 2009a and b).

Drilling that occurred in Site C0006 and did not reach the underthrust sediments due to drilling conditions. Unlike Site C0006, drilling at Site C0007 went through the slope, prism, and underthrust sediments. The general lithology between the two sites is similar and can be separated into four units. Unit I, the slope sediments, contains fining-upward successions of silty clay, sand, sand silt, and rare volcanic ash layers. Unit II, the accreted trench wedge, is a succession of coarsening-upward clay to sand and gravel. Unit III, the Shikoku Basin facies, is composed of mudstone with volcanic ash layers. Lastly, Unit IV, the underthrust trench wedge, is primarily composed of sand that

is presumably young in age, although poor recovery prevented dating (Expedition 316 Scientists 2009a, b) (Figures 2-4, 2-5, and 2-6).

Expedition 322 drilled into the incoming sediments, including the basement, at Sites C0011 and C0012 (Figures 2-2, 2-7, and 2-8). The drilling at Site C0011 was planned to drill into the basalt, but due to complications and time shortage, the basement was not reached. The drilling started at ~340 mbsf, not coring the upper Shikoku Basin facies, and the drilling stopped at 950 mbsf. Expedition 333, conducted in December 2010 through January 2011, returned to Sites C0011 and C0012 to complete the record at these sites and collect temperature data. The report for this expedition has not yet been released.

Site C0012 is located on a basement high, known as the Kashinosaki Knoll (Figure 2-2). Because of the location, all the units within Site C0012 are thinner than those of Site C0011 and the basement was able to be drilled at 537 mbsf. Unit I, the upper Shikoku Basin facies was not cored and the description is inferred from ODP Sites 808, 1173, 1174, and 1177. It is composed of hemipelagic mud with interbedded volcanic ash. Unit II, the middle Shikoku Basin facies is Miocene in age and ranges from silty claystone with interbedded sandstone to silty claystone, volcanoclastic sandstone and siltstone. Unit III, the lower Shikoku is middle to late Miocene in age and is mainly composed of silty claystone. Unit IV, the lower Shikoku: turbidites are middle Miocene in age and are composed of silty claystone with interbedded clayey siltstone and siliciclastic sandstone. These LSB sandstones are similar to those described at the Ashizuri transect. Due to its location Site C0011 contains a greater number of sand layers from gravity flows and turbidity currents than Site C0012. Unit V, the

volcaniclastic-rich facies ranges in the middle Miocene and is primarily composed of silty claystone and tuff with sandy siltstone. Unit VI, which was only recovered in Site C0012, is a pelagic clay facies from the early Miocene in age (Underwood et al. 2009).

Pore fluid from samples obtained from Site C0011 greater than 600 mbsf, which is in the LSB, had chloride (Cl<sup>-</sup>) concentrations that were 7% lower than seawater concentration. Underwood et al. (2009) suggested this fluid found at Site C0011 could originate from clay dehydration from depth and the fluid arrived at Site C0011 through permeable layer in the Lower Shikoku Basin sandstones. Also, hydrocarbon concentrations, such as propane, were found to increase with depth at Site C0011 (Figure 2-2). Unlike Site C0011, the Cl<sup>-</sup> concentration at Site C0012 increases by 12% with no indications of freshening, and propane was absent throughout the core. The lack of propane and Cl<sup>-</sup> freshening signal suggests the influence of fluids from depth did not reach Site C0012 (Underwood et al., 2009). Low chloride concentrations have been observed within the LSB at Site 1177 seaward of the deformation front along the Ashizuri transect.

Porosity-depth profiles are available from the drilling results of both Sites C0011 and C0012. Porosity is an important indication of the compaction state of sediments. The incoming sediments contain a decreasing trend of porosity with depth, which is typical of sediment consolidation (Underwood et al., 2009). When comparing the porosity-depth profile of the lower Shikoku Basin facies from the Kumano Basin transect to the Muroto transect, the profiles contain a similar trend in consolidation (Figure 2-9).

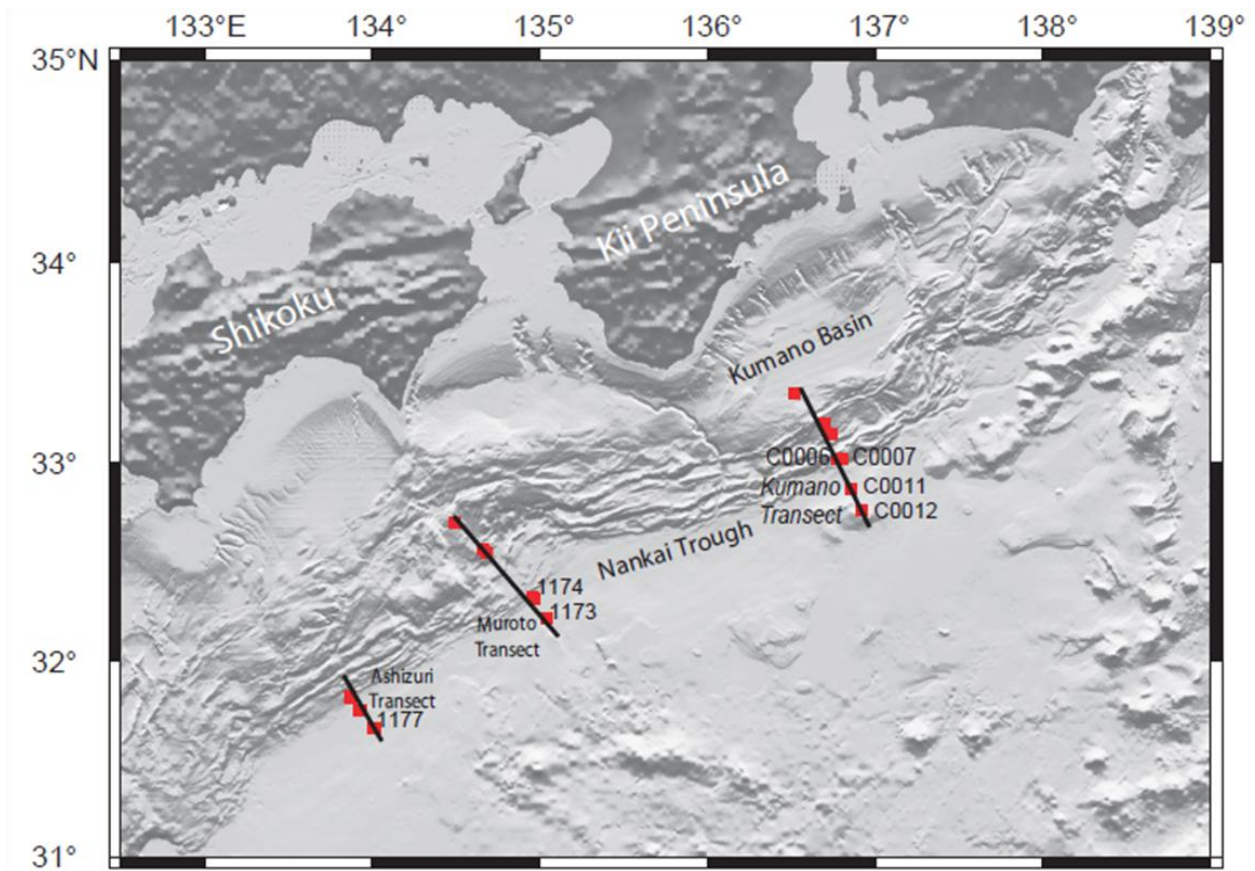


Figure 2-1. A map depicting the Ashizuri, Muroto, and Kumano Basin transects.

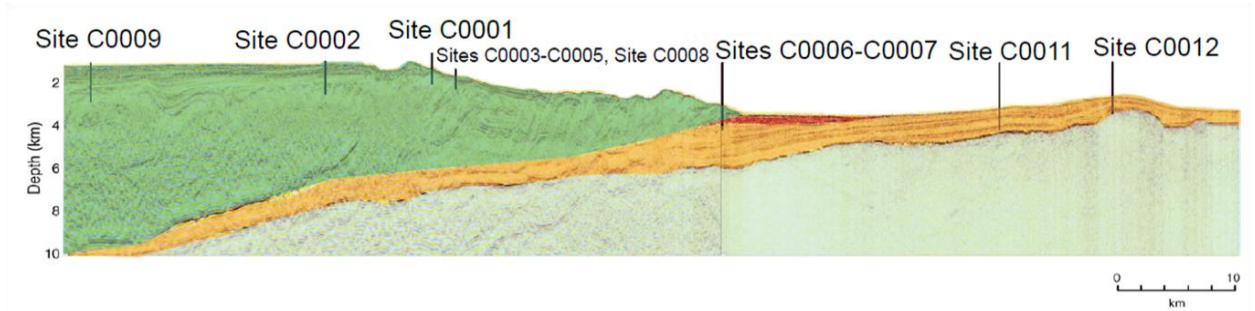


Figure 2-2. The seismic profile of the Kumano Basin transect (modified from Underwood et al. 2009 and based on the interpretations of Moore et al., 2009). Sites C0006, C0007, C0011, and C0012 are the primary focus within this investigation.

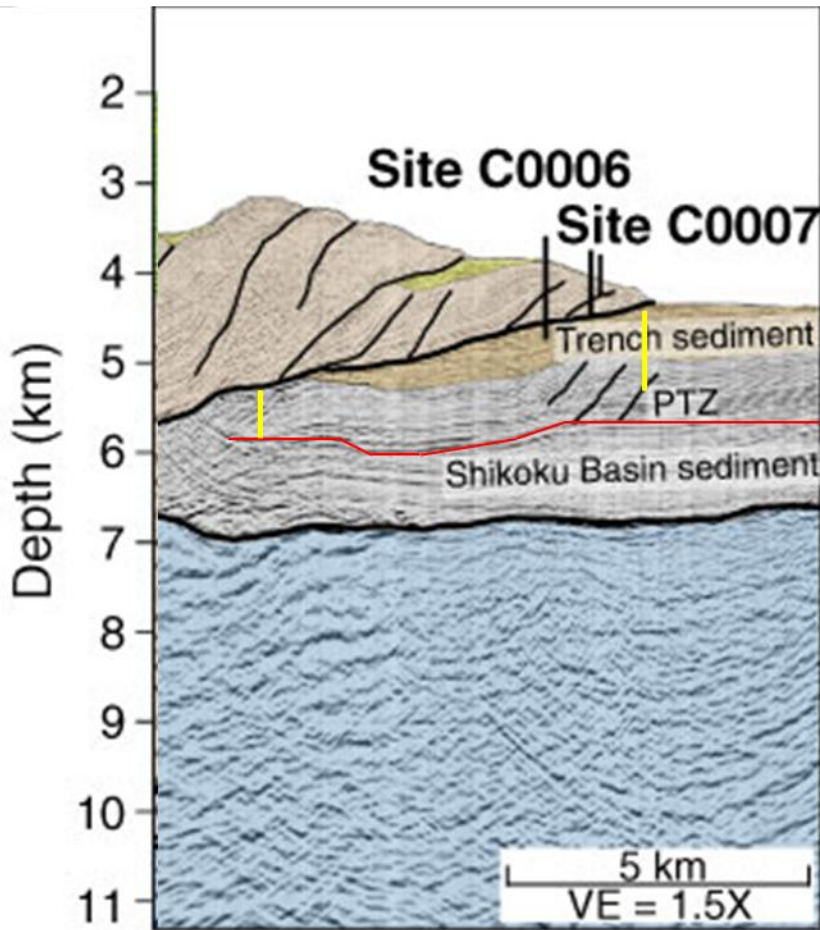


Figure 2-3. The frontal thrust region of the Kumano Basin transect, with the inferred protodécollement (in red) and the locations of profiles at the trench and 7 km from the trench (in yellow) (modified from Moore et al., 2009).

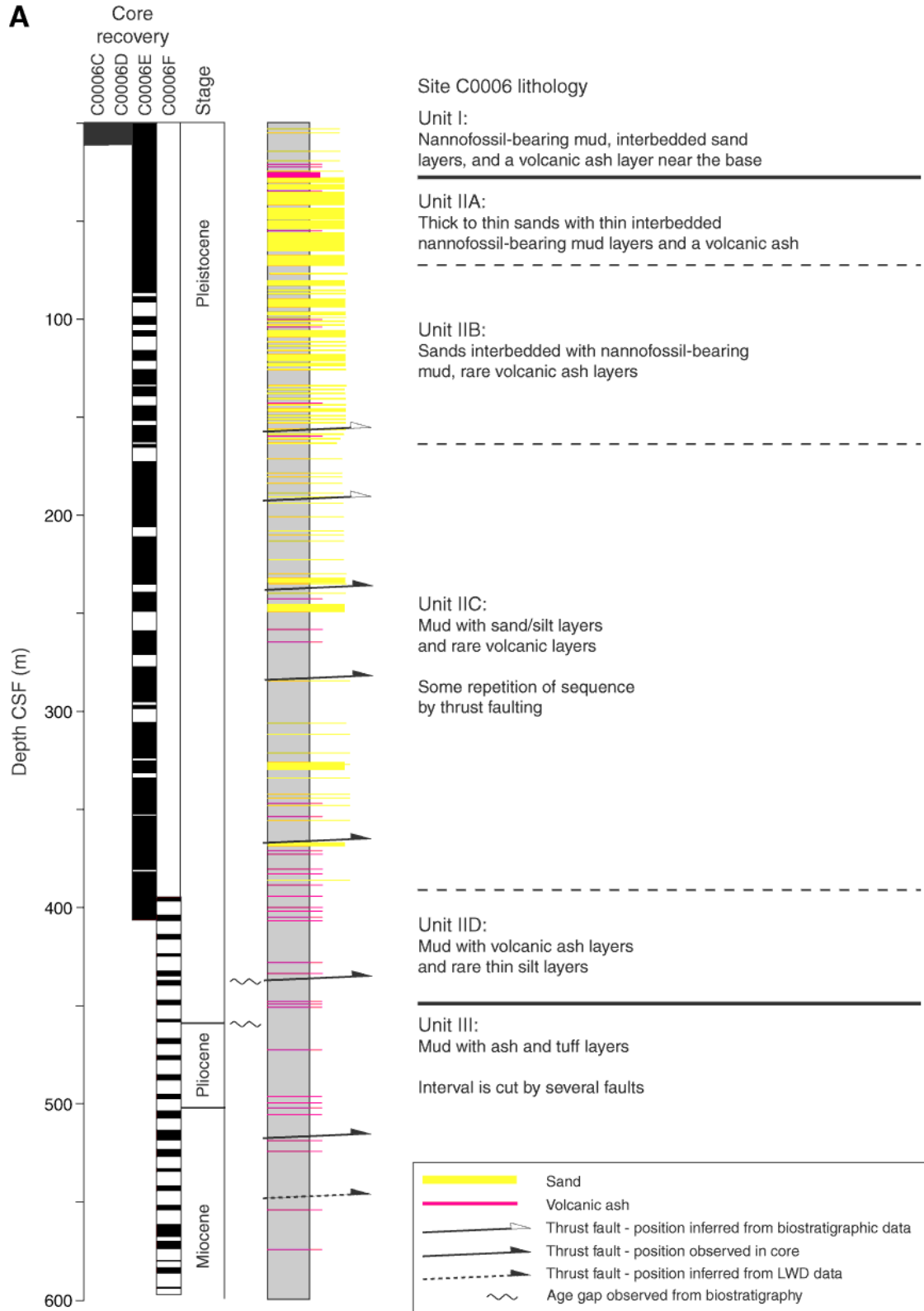


Figure 2-4. The stratigraphic profile of Site C0006 (Expedition 316 Scientists, 2009a).

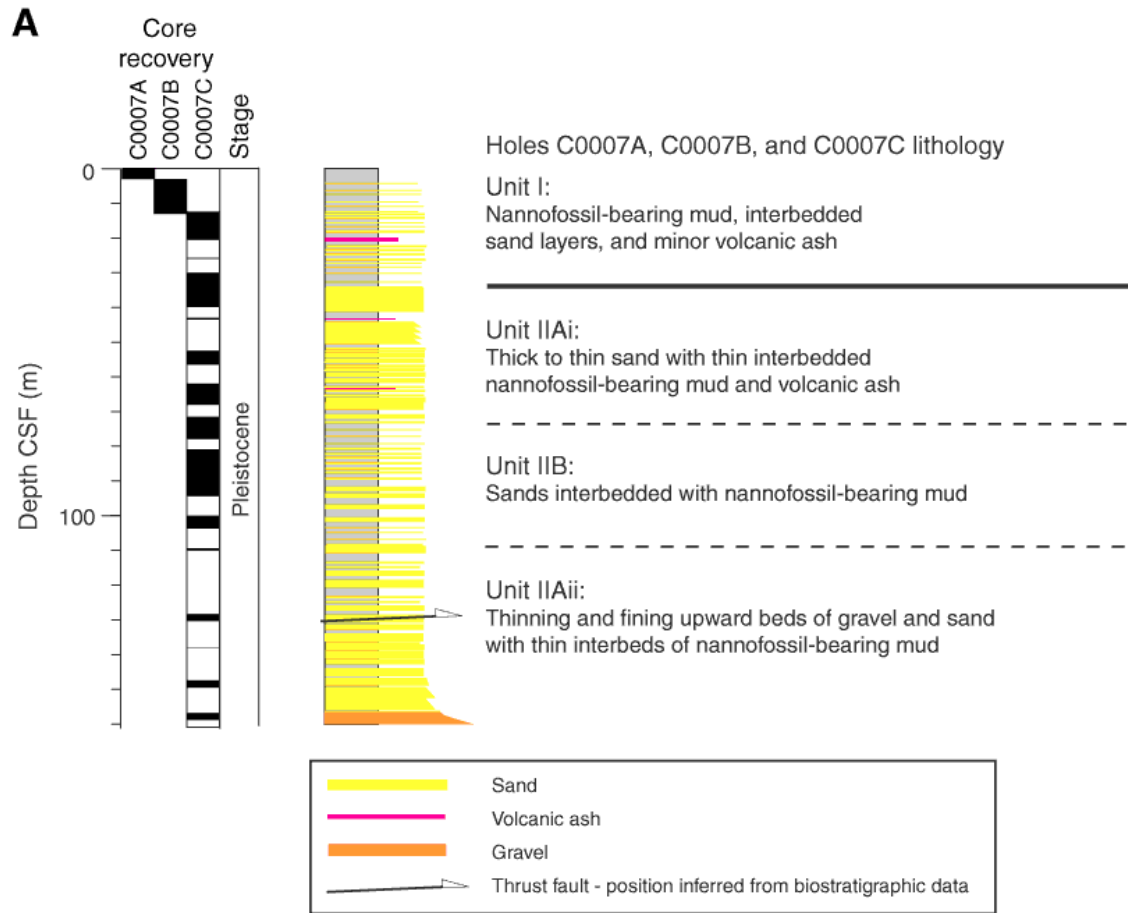


Figure 2-5. The stratigraphic profile for Site C0007 (Expedition 316 Scientists, 2009b).

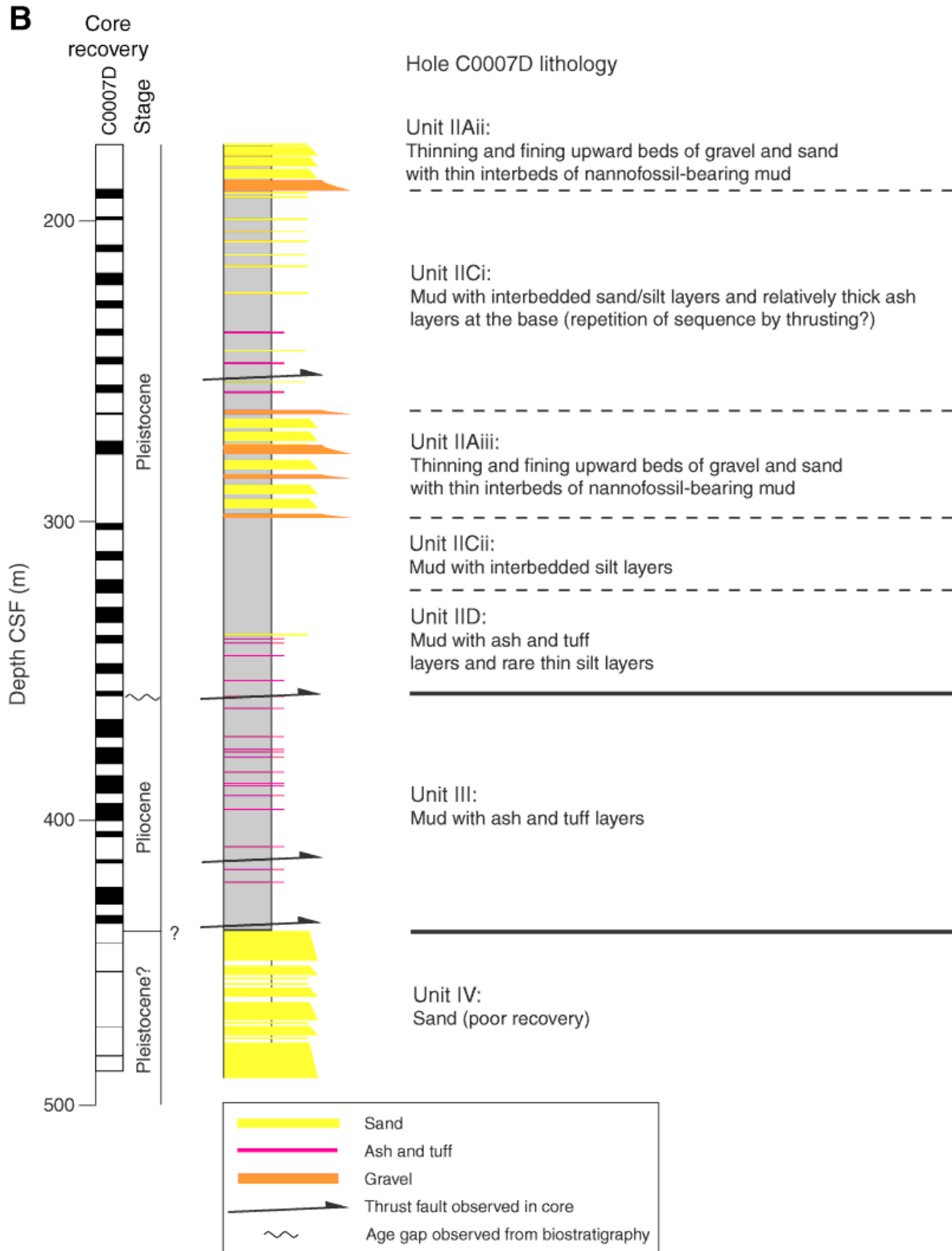


Figure 2-6. The stratigraphic profile for Site C0007 (Expedition 316 Scientists, 2009b).

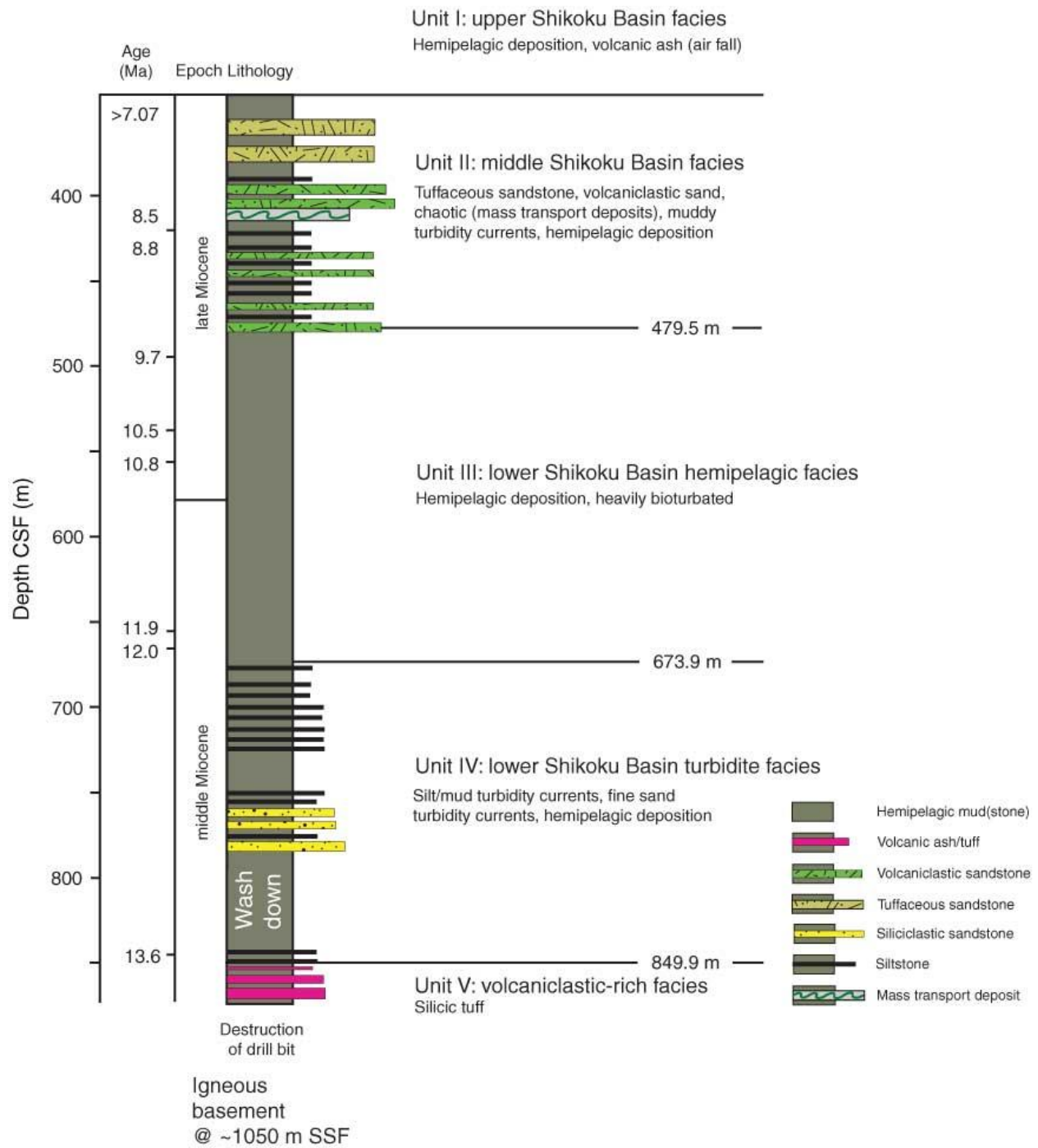


Figure 2-7. The stratigraphic profile of Site C0011 (Underwood et al., 2009)

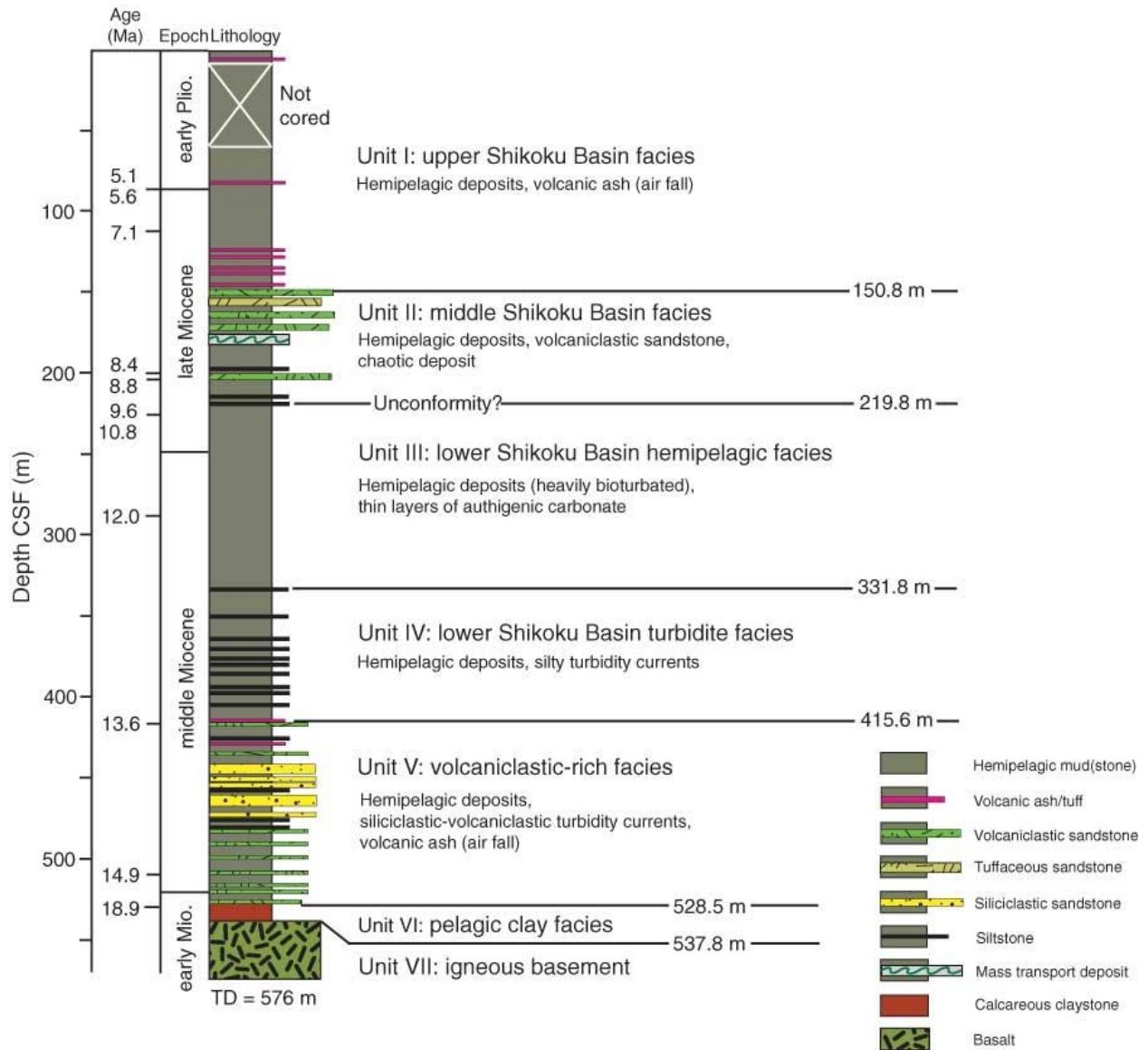


Figure 2-8. The stratigraphic profile of Site C0012 (Underwood et al., 2009).

# POROSITY-DEPTH PROFILE

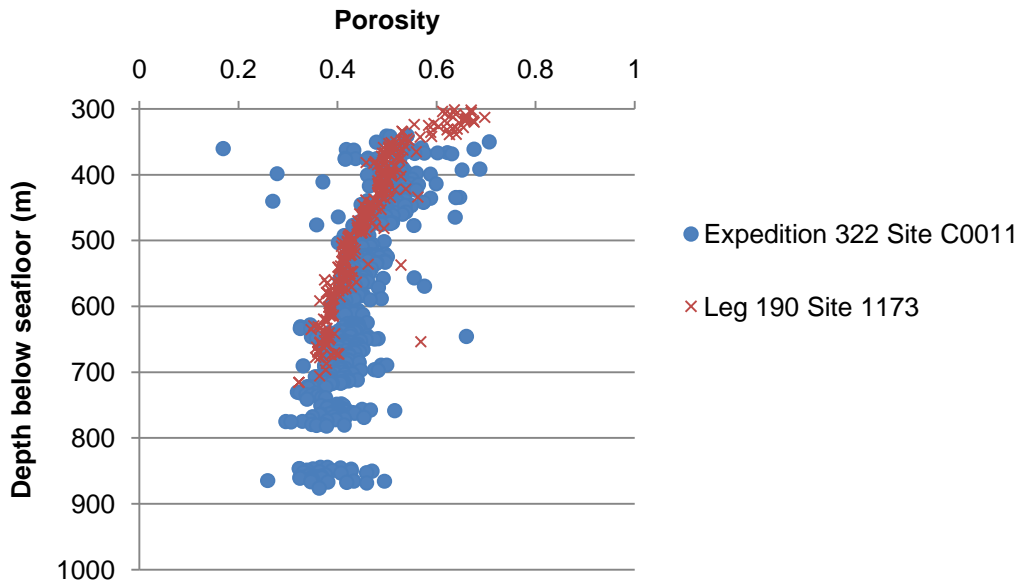


Figure 2-9. The porosity-depth profiles from the incoming sediments of the Kumano Basin (Expedition 322) and Muroto (Leg 190) transects.

CHAPTER 3  
EQUATIONS OF FLUID FLOW AND DEFORMATION

**Fluid Flow**

Fluid flow is governed by Darcy's Law which expresses the relationship between fluid and sediment properties, hydraulic head, and fluid velocity:

$$v_f = - \left[ \left( \frac{k \rho_f g}{n_e \mu} \right) \nabla h \right] \quad (3-1)$$

where  $v_f$  (m/s) is the velocity of fluid flow,  $k$  ( $m^2$ ) is the permeability,  $\rho_f$  ( $kg/m^3$ ) is fluid density,  $g$  ( $m/s^2$ ) is gravity,  $n_e$  is the effective porosity,  $\mu$  ( $kg/ms$ ) is the viscosity of the fluid, and  $h$  (m) is hydraulic head (Domenico and Schwartz, 1998). Hydraulic head can be expressed in terms of pore pressure (P):

$$h = \left[ \frac{P}{\rho_f g} + z \right] \quad (3-2)$$

where  $z$  (m) is the elevation head and  $P$  (Pa) is the pore pressure. The groundwater governing equation is created by combining Darcy's Law in terms of pore pressures with the conservation of mass equation (Ingebritsen et al., 2006; modified by Sreaton, 2010):

$$\nabla \cdot \left[ \frac{k \rho_f}{\mu} (\nabla P + \rho_f g \nabla z) \right] + R_m = \frac{\partial (n p_f)}{\partial t} \quad (3-3)$$

where  $t$  (s) is time,  $n$  is porosity, and  $R_m$  ( $kg/m^3s$ ) is a fluid source term.

Permeability describes the ease of fluid flow through a porous material and can vary by orders of magnitude for different sediment types. A relationship between the logarithm of permeability and porosity of clays was developed by Bryant et al. (1975) and Neuzil (1994):

$$\log(k) = \log(k_0) + \gamma n \quad (3-4)$$

Where  $\log(k_0)$  is the logarithm of permeability extrapolated to zero porosity, and  $\gamma$  is the slope of the porosity-permeability relationship. Hydraulic conductivity (K) (m/s) combines the fluid properties and the permeability:

$$K = \frac{k\rho_f g}{\mu} \quad (3-5)$$

Temperature can affect fluid flow by altering fluid viscosity (Voss and Provost, 2010):

$$\mu(T) = (239.4 \times 10^7) \left(10^{\frac{248.37}{T+133.15}}\right) \quad (3-6)$$

### **Elastic and Poroelastic Deformation**

In a deforming porous material, fluid pressures and flow are closely related to strain and stress. A linear elastic strain is proportional to the applied stress and will

revert back to the original state once the stress is relieved. The relationship between stress and strain for two dimensions can be expressed as:

$$\varepsilon_{xx} = \frac{1}{E} [\sigma_{xx} - \nu(\sigma_{yy})] \quad (3-7)$$

$$\varepsilon_{zz} = \frac{1}{E} [\sigma_{yy} - \nu(\sigma_{xx})] \quad (3-8)$$

where  $\sigma_{xx}$  (Pa) is the stress in the horizontal direction,  $\sigma_{zz}$  (Pa) is the stress in the vertical direction,  $\varepsilon$  is the strain,  $\nu$  (unitless) is Poisson's Ratio, and  $E$  (Pa) is Young's Modulus.  $E$  is the incompressibility or stiffness of the rock, while  $\nu$  is the ratio of compression and thickening (Ingebritsen et al., 2006).

In porous materials, pore pressure cannot be ignored. Pore pressure is related to stress through the effective stress principal in the poroelasticity theory. The change in total stress ( $\sigma$ ) is related to the change in pore pressure and the change in the effective stress felt within a porous media ( $\sigma_e$ ):

$$\Delta\sigma = \Delta\sigma_e + \left[1 - \frac{a_s}{a_b}\right] \Delta P \quad (3-9)$$

where  $a_s$  is the compressibility of the mineral grains ( $\text{ms}^2/\text{kg}$ ) and  $a_b$  is the bulk compressibility of the porous medium:

$$a_s = \frac{\Delta V}{V\Delta\sigma_e} \quad (3-10)$$

$$a_b = \frac{\Delta V_s}{V_s \Delta \sigma_e} \quad (3-11)$$

where  $V$  is the total volume and  $V_s$  is the volume of the solids (Ingebritsen et al., 2006; Screatton, 2010). Bulk compressibility ( $a_b$ ), Young's Modulus, and Poisson's Ratio are related through a linear relationship (Wang, 2000):

$$a = \frac{E}{3(1-2\nu)} \quad (3-12)$$

If the bulk compressibility of the porous medium is significantly greater than the bulk compressibility of the grains ( $a_b \gg a_s$ ), Equation 9 simplifies to:

$$\sigma = \sigma_e + P \quad (3-13)$$

To tie everything together, fluid flow in terms of pore pressures is coupled with deformation in terms of effective stress:

$$\nabla \cdot \left[ \frac{k \rho_f g}{\mu} (\nabla P + \rho_f g \nabla z) \right] + R_m g = S_{s3} \frac{\partial P}{\partial t} - S_{s3} B \frac{\partial \sigma}{\partial t} \quad (3-14)$$

where  $S_{s3}$  (1/m) is the specific storage in three-dimensions and  $B$  is Skempton's Coefficient:

$$S_{s3} = \rho_f g [(a_b - a_s) + n(a_f - a_s)] \quad (3-15)$$

$$B = \frac{a_b - a_s}{(a_b - a_s) + n(a_f - a_s)} \quad (3-16)$$

where  $n$  (dimensionless) is the porosity and  $a_f$  ( $\text{ms}^2/\text{kg}$ ) is the compressibility of the fluid (Screaton 2010).

### **Plastic Deformation**

For large strains, most sediments are plastic rather than elastic, and will not return to their original undeformed shape once the applied stress is removed. To characterize the stress and strain behaviors of soils, Roscoe and Burland (1968) and Schofield and Wroth (1968) developed the Cam Clay and Modified Cam Clay models. The Modified Cam Clay model is based on the ability to predict volume changes of a material due to loading, or the plasticity theory. The Modified Cam Clay model is designed to simulate the behavior of soils by predicting the pressure-dependent soil strength and the change in volume and compression caused by applying a shear stress ( $\sigma_s$ ) or stress tangential or parallel to the surface. The modified Cam Clay model allows calculation of the deformation or compaction of a solid during loading (Helwany, 2007).

To find the Cam Clay parameters for a material, a triaxial test or a one-dimensional consolidation test can be performed on a sample and results plotted along an  $e$ - $\log(\sigma'_v)$  plot (Figure 3-1). For one-dimensional consolidation,  $\log(\sigma'_v)$  is the log of the effective vertical stress and  $e$  is the void ratio ( $e=n/(1-n)$ ). The break in the slope on Figure 3-1 is the effective stress above which the material begins to deform plastically. The consolidation curves are used to find the compression and swelling index from the slope. The compression index ( $C_c$ ) is the slope of the loading curve,

while the swelling index ( $C_s$ ) is the slope of the unloading curve that reflects the elastic rebound when the effective stress is reduced (Figure 3-1). As an alternative to laboratory experiments, field data can be used to relate observed void ratio and effective stresses to find the compression index. The Cam Clay parameters,  $\Lambda$  and  $\kappa$ , are related to  $C_c$  and  $C_s$  (Helwany, 2007):

$$\Lambda = \frac{C_c}{2.3} \quad (3-17)$$

$$\kappa = \frac{C_s}{2.3} \quad (3-18)$$

### Friction

Slip along a fault occurs when the shear stress (the stress that is parallel or tangential to a surface), is greater than the frictional strength. Coulomb's failure relationship describes the failure under stress conditions, and describes the slip tendency:

$$\sigma_c = \sigma_s + \chi(\sigma_n + P) \quad (3-19)$$

where the  $\sigma_c$  is the tendency for slip,  $\chi$  is the coefficient of friction, and  $\sigma_n$  is the normal stress or the stress perpendicular to a surface. If  $\sigma_c$  is positive, there is an increased tendency for the fault to slip, whereas if  $\sigma_c$  is negative, there is a decrease in the tendency for the fault to slip (King et al., 1994; Masterlark and Wang, 2000; Hughes et al., 2010).

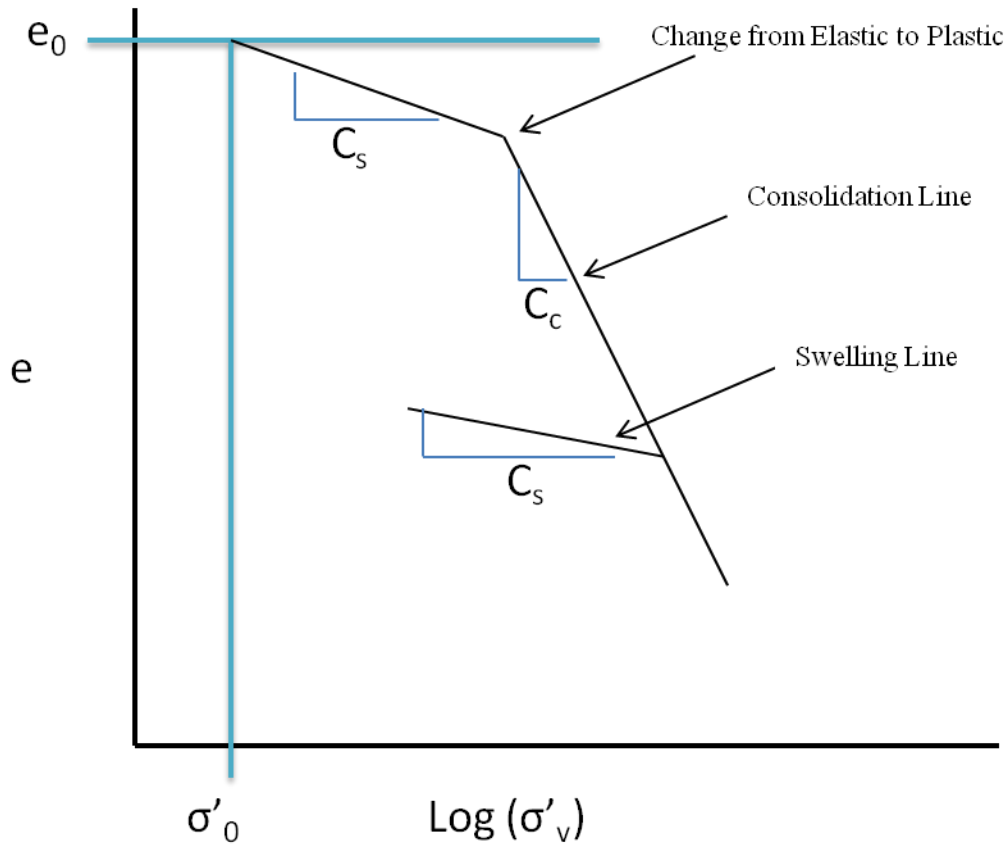


Figure 3-1. A representation of consolidation curve and the swelling curve (modified from Helwany, 2007).

## CHAPTER 4 PREVIOUS NANKAI INVESTIGATIONS

Based on data and samples from the Muroto transect, excess pore pressures have been estimated (Screaton et al., 2002; Saffer, 2003) and the permeability-porosity relationship of the Shikoku Basin Clay calculated (Saffer and Bekins, 1998; Gamage and Screaton, 2006; Skarbek and Saffer, 2009). Screaton et al. (2002) used the measured porosity along the Muroto transect to estimate the excess pore pressure within the proto-underthrust sediments (Site 1174) and underthrust sediments (Site 808). Assuming hydrostatic pore pressure ( $P_L^* = \sigma_e$ ) within Site 1173, they created a porosity versus effective stress relationship. Using this relationship as a reference, they compared it to the porosity versus the excess lithostatic stress at Sites 808 and 1174, to calculate the pore pressures at these two sites. Screaton et al. (2002) calculated the pore pressure ratio,  $\lambda^*$ , as the excess pore pressure ( $P^*$ ) divided by the excess lithostatic pressure ( $P_L^*$ ):

$$\lambda^* = \frac{P^*}{P_L^*} = \frac{P - P_H}{P_L - P_H} \quad (4-1)$$

The lithostatic pressure ( $P_L = \rho_b z$ ) can be described as the pressure of the overlying body, and  $P_H$  is the hydrostatic pressure (Screaton et al., 2002). For Site 1174, Screaton et al. (2002) estimated a  $\lambda^*$  of ~0.42 and for Site 808, a  $\lambda^*$  of ~0.47. These results suggest underconsolidation of the sediments, potentially due to rapid loading of the low permeability sediments.

Saffer (2003) used a similar method but included laboratory consolidation experiments, logging while drilling (LWD), and void ratio reduction to estimate pore pressure development within underthrust sediments at Sites 1173 and 808. His results were similar to but slightly lower than the results of Screaton et al. (2002), yielding a Site 1174 protodécollement  $\lambda^*$  of  $\sim 0.34$  and Site 808 décollement  $\lambda^*$  of  $\sim 0.44$ .

The permeability-porosity relationship (Equation 16) has been estimated based on inverse numerical modeling (Saffer and Bekins, 1998) and laboratory tests on Muroto and Ashizuri core samples (Gamage and Screaton, 2006; Skarbek and Saffer, 2009; Saffer 2010). Saffer and Bekins (1998) calculated the first permeability-porosity relationship for the Muroto transect based on inverse modeling (Table 4-1). Gamage and Screaton (2006) used a constant flow method to calculate the vertical permeability and create a permeability-porosity relationship. The Gamage and Screaton (2006) relationship contains the highest permeability intercept. Skarbek and Saffer (2009) and Saffer (2010) created a log-linear relationship between the porosity and permeability measured during constant rate of strain uniaxial consolidation testing (CRS). Saffer (2010) and Skarbek and Saffer (2009) found their relationship was steeper but consistent with Gamage and Screaton (2006) (Table 4-1).

General patterns of subduction zone permeability-porosity relationships were investigated further by Gamage et al. (2011) by compiling the available permeability-porosity data from siliciclastic samples from Barbados, Nankai, Peru, and Costa Rica; they found that grain size distribution is the most important control on the permeability-porosity trend. Their results illustrated a general trend of increase in permeability with a

decrease in clay size particles at any given porosity, despite different locations and thermal conditions.

### **Previous Nankai Trough Modeling**

The evolution of pore pressure within a subduction zone and the influence of other parameters, such as morphology of the prism, potential heat transport, chemical transport, fault strength, and sediment strength have been investigated on several convergent margins (Saffer and Bekins, 1998; Stauffer and Bekins, 2001; Saffer and Bekins, 2002; Saffer, 2003; Saffer and Bekins, 2006; Saffer, 2007). Specifically, modeling of the pore pressure and fluid flow within the Nankai margin has been performed by multiple scientists (Gamage and Scretton, 2006; Skarbek and Saffer, 2009; Saffer, 2010).

Gamage and Scretton (2006) used laboratory permeability data to investigate porosity and excess pore pressure in the Muroto Transect. They incorporate one-dimensional modeling of loading into a fluid flow model by increasing the pore pressure by the added weight of effective overburden. Gamage and Scretton (2006) simulated results for Sites 1174 and 808  $\lambda^*=0.14$  and  $0.22$ , respectively, which were lower than the previous findings of Scretton et al. (2002) and Saffer (2003). If excess pore pressures are as high as Scretton et al. (2002) and Saffer (2003) observed beneath the frontal thrust, then the permeabilities must be lower due to a low permeability barrier above the décollement, a lower bulk permeability, or both (Gamage and Scretton 2006).

Skarbek and Saffer (2009) used laboratory permeability measurements and one-dimensional model of loading to investigate the evolution of pore pressure within the underthrust sediments of the Muroto transect from shallow to great depth. Their

approach is similar to the approach of Gamage and Sreaton (2006), except Skarbek and Saffer (2010) include a pressure “cap” at the décollement. Their modeling yielded an average pore pressure ratio,  $\lambda^*$ , of 0.50 at Site 1174 and  $\lambda^*$  of 0.30-0.60 along the décollement up to 20 km landward of the trench.

Saffer (2010) used a two dimensional model to compare and understand the fluid flow of the Muroto and Ashizuri transect. He simulated compaction by computing the fluid released from compaction and dehydration for a reference frame fixed at the deformation front. He found that the lithostratigraphy influences the mechanical behavior of subduction zones by affecting the distribution and magnitude of excess pore pressure. He calculated the average basal pore pressure ratio for 30 km. The modeling yielded a  $\lambda^*$  of  $\sim 0.59$  for the Muroto transect and a  $\lambda^*$  of  $\sim 0.38$  for the Ashizuri transect (estimated from Figure 8 in Saffer, 2010). The underthrust sediments were found to dewater in the Ashizuri transect through the LSB sandstone. This dewatering resulted in lower excess pore pressure ratios, by  $\sim 15\%$ , in the Ashizuri transect as compared to the Muroto transect, which lacks the buried LSB sandstone.

### **Previous Fully Coupled Subduction Zone Fluid and Deformation Models**

Due to the data needs and difficulty, fully coupled deformation-fluid flow models are less commonly applied than the partially coupled models discussed above. Finite Element Models (FEMs) have been used to understand the influence of fully coupled deformation and fluid flow (Hughes et al., 2010; Masterlark and Hughes, 2008). Hughes et al. (2010) illustrated the importance of pore pressures and elastic behavior within the subduction zone off the coast of Sumatra using a FEM, Abaqus. Stauffer and Bekins (2001) investigated mechanisms that prevented consolidation and maintained high permeability along the décollement of the northern Barbados accretionary complex.

Using a coupled fluid flow/consolidation model that included the modified Cam Clay relationship, they found high pore pressures migrated seaward of the deformation front, consistent with the underconsolidation inferred from high porosities in sediment cores. The simulations depicted minor swelling in the incoming sediments up to 3 km before subduction, which could explain shear and faulting proximal to the protodécollement (Stauffer and Bekins, 2001).

Table 4-1. Log-linear permeability-porosity relationships of the Shikoku Basin clay estimated from core samples from the Muroto transect or inverse modeling.

Reference	Relationship
Saffer (2010)	$\log(k) = -20.45 \pm 0.5 + 6.93n$
Skarbek and Saffer (2009)	$\log(k) = -20.45 + 6.93n$
Gamage and Screatton (2006)	$\log(k) = -19.82 + 5.39n$
Saffer and Bekins (1998)	$\log(k) = -20 + 5.5n$

## CHAPTER 5 MODEL DESIGN

### **Modeling Approach**

We use the FEM package Abaqus ([www.simulia.com](http://www.simulia.com)) which includes coupled fluid flow and deformation for soil mechanics. With Abaqus, the design of a model can be in two or three dimensions, with no restrictions on the overall shape. Displacement of the nodes allows the calculation of stress and strain, which affects the other variables within the element (Abaqus 6.7, 2007). We include the influence of lithostratigraphy of the region by using permeability-porosity data from samples of Expeditions 316 and 322 and literature, consolidation parameters from previous investigations of the Muroto transect and the observed porosity data of the incoming sediments, and a thermal profile to simulate the effects of temperature-dependent viscosity on hydraulic conductivity. Modeling does not incorporate the effects of dehydration reactions, such as the smectite-illite transition. This was excluded due to the findings of Saffer and Bekins (1998), who found minimal influence the dehydration on fluid pressure for the Muroto transect and Bekins et al. (1995) who found that the dehydration-driven fluid sources are small when compared to the compaction-driven sources for simulation of the Barbados subduction zone.

### **Modeling Setup**

Our model is composed of the prism, the trench sediments, the Shikoku Basin Clay, the Lower Shikoku Basin (LSB) sandstone, and basalt layer. The entire modeled region is 73 km long, 23 km landward from the trench (prior to displacement) and 50 km seaward from the trench. The prism is ~5 km thick at the most landward location. The incoming Shikoku Basin facies is ~1.4 km thick (after compaction), and includes the

LSB sandstone that is simulated as ~0.4 km thick. The trench sediment contains a maximum thickness of 0.5 km extending from ~7km beneath the prism to 10 km seaward of the prism. Due to the difficulties of the coupled modeling, some simplifications were made to the geometry. In reality, the prism does not start on top of the trench sediments. Furthermore, the trench sediments are deposited as the subduction is occurring. Lastly, the trench sediments are about half the observed thickness of 1 km. The upper 3 km of basalt is included in the model as its strength was found to be important to the deformation of the region (Figure 5-1). The mesh is composed of 4218 quadrilateral elements and 4722 nodes. The frontal thrust is represented as an interaction between two parts, the prism and the footwall (including the trench turbidites, the Shikoku Basin clay, and the LSB sandstone), and is assigned a coefficient of friction.

Hydrostatic pore pressure is applied to the top of the model to represent the bottom of the ocean. We also apply a hydrostatic boundary along the right-hand side of the model. The bottom of the model is constrained to have no vertical movement, while the left and right side of the footwall are constrained to have no horizontal movement. To test the sensitivity of the hydrostatic boundary on the seaward side of the footwall, we removed the boundary condition creating a no flow boundary. A simulation with the seaward footwall able to move horizontally was created to see the sensitivity of the no movement boundary. Each resulted in minimal influence (~1%) on simulated excess pore pressures.

### **Modeling Procedure**

Due to temperature influencing the fluid flow viscosity, an initial model simulation of thermal conduction was run to develop a distribution of temperatures throughout the

model region. The top of the model is set to 2°C, based on the temperature data of seawater from Expedition Scientists (2009a, b). With the input of heat flow, based on measured temperatures and inferences from bottom simulating reflectors (Kinoshita et al., 2008), and average thermal conductivity for each of the model lithologies (Kinoshita et al., 2008; Expedition 316 Scientists, 2009a and b), Abaqus calculated the temperatures based on thermal conduction (Figure 5-2).

Prior to movement of the frontal thrust, gravity was applied to each part of the model as a body force, based on the acceleration due to gravity ( $g=9.81$  m/s) and the average effective density of the rock (bulk density of the rock minus the density of salt water) in each of the model lithologies. The body force was applied gradually over 4 million years to create starting conditions for frontal thrust movement. Following the initial equilibration with the body force, we displaced the left side of the accretionary prism 7.2 km to generate a toe movement of about 6 km after prism shortening. The displacement was applied for the duration of 0.61My, which is the middle of the range of age estimates for frontal thrust initiation (Screaton et al., 2009). Because the actual displacement history is not known, we assume a constant frontal thrust slip velocity throughout the model. As the prism moves seaward, a pressure is applied to the exposed region of the footwall to compensate for the removed body of the prism.

### **Modeling Parameters**

The five specific regions of the model are assigned mechanical and fluid flow parameters. Each part of the model has a unique permeability-porosity relationship. Basalt permeability varies with depth and ranges vastly. In previous studies at other locations, the regional-scale permeability for the upper basement aquifer, which is composed of sheet flows and pillow basalt, has been constrained by pressure transient

borehole tests and the thermal state of the basalt to range from  $1 \times 10^{-19}$  to  $1 \times 10^{-10} \text{ m}^2$  (Becker and Davis, 2004; Davis et al., 2000; Davis and Becker, 2002; Fisher, 2005). Kummer and Spinelli (2009) note variations of permeability with depth and the lack of knowledge concerning how lateral permeability changes during subduction. Underwood et al. (2009) found evidence for circulation in upper basement at C0012 but note that it is hydrologically isolated from the sediments. To prevent high rates of drainage of the sediments into the basalt, contrary to the Site C0012 observations, we assign a permeability value of  $1 \times 10^{-17} \text{ m}^2$ .

The permeability-porosity relationships of the prism and the Shikoku Basin clays are taken from the data results of Sites C0006 and C0007 and previous permeability results presented below. To obtain permeability-porosity data for the Kumano Basin transect, we measured the vertical permeability and porosity of nine core samples from Sites C0006 and C0007 using the flow-through system described by Gamage and Screatton (2003). Detailed methods and results of the laboratory tests are provided by Rowe et al. (in review). Fluid flow was driven by generating a known difference in pressure at the top and bottom of the sample and flow rate was measured. Using Darcy's Law, the hydraulic conductivity was calculated for each sample, which was then converted into permeability based on fluid properties at laboratory temperature. Using porosity data from Expedition 316, the change in porosity was calculated at each effective stress, which is based on the change in fluid volume in the cell.

We use the permeability-porosity relationship of the LSB sandstone measured by Hüpers et al., (in review),  $\log(k) = 6.6108n - 17.71$ . The trench sediments are simulated to be a combination of sand, gravel, and clay. To develop a permeability-porosity

relationship for this layer, we combined the known clay relationship, with generic sand permeability (Schwartz and Zhang, 2003). Heterogeneous vertical hydraulic, between two lithological layers is calculated by dividing the total thickness by the sum of the each thickness layer divided by the hydraulic conductivity:

$$K_v = \frac{\text{total thickness}}{\frac{\text{layer 1 thickness}}{K_{v1}} + \frac{\text{layer 2 thickness}}{K_{v2}}} \quad (5-1)$$

Due to the trench sediments being sandy to clayey sandy, we estimated half the trench to be clay and half to be sand, and developed a permeability-porosity relationship for the trench sediment yielding  $\log(k) = -19.444 + 6.8851n$ .

The décollement and frontal thrust are not assigned a specific permeability because of its location and the shallow design of our model. The frontal thrust abuts the sand-rich trench sediments. This sand-rich layer provides a channel in which fluid can escape from beneath the prism. Thus assigning high permeability to the fault zone is unnecessary for our shallow region.

For elastic portions of the model, the Young's Modulus (E) or stiffness and the Poisson's Ratio ( $\nu$ ) are two parameter needed for compaction calculations. Masterlark (2003) used a Poisson's Ratio of 0.3 for the oceanic crust based on data compiled by Turcotte and Schubert (1982) who found the common crustal rock Poisson's ratio ranged from 0.1-0.4, while Christensen (1996) depicted the range of bulk representation of crust to range from 0.25-0.32. We use a Poisson's Ratio of 0.3 throughout the model.

The prism is treated as elastically based on the conclusion of Moore et al. (2009) who suggested that the prism has come up from depth. Thus the applied effective stresses are expected to be less than those previously experienced through burial, and the deformation will be elastic. In addition, the focus in our simulations is on the footwall

rather than the prism because the excess pore pressure primarily occurs within the footwall in previous investigations (Screaton et al., 2002 and Saffer, 2003). We used  $E=5 \times 10^8$  Pa for the prism. In Abaqus, during the displacement of the prism, if the prism is too stiff, the model fails. The chosen stiffness is the maximum Young's Modulus that can be applied without the model failing. This stiffness is a little high for clay but is representative of sandy gravel based on the compressibility found in Domenico and Schwartz (1998). The basalt is treated as elastic. Based on the literature values of compressibility given in Domenico and Schwartz, (1998), we apply an  $E$  of  $5 \times 10^{11}$  Pa for the basalt.

We apply the Cam Clay parameters to the Shikoku Basin clay, LSB sandstone, and trench sediments. The compression-swelling (elastic values) line ( $\kappa$ ) and virgin or primary compression line ( $\Lambda$ ) values were initially based on the results of consolidation tests performed on Muroto transect samples (Bellew, 2004). Results from samples of the Kumano Basin transect are not yet available. Despite the thermal differences between the Muroto and Kumano Basin transects, the similarities between the porosity-depth profiles of the incoming sediments suggest that they share a similar consolidation behavior (Figure 2-9). The appropriateness of the laboratory data was checked by comparing the simulated porosities of the incoming sediments to those measured at Site C0011. The value derived from the laboratory test underestimated compaction. To better match the field data, the  $\Lambda$  value was increased to 0.3.

Cam Clay parameters of the sand-rich sediments are not available. For trench sediments, we applied the Cam clay parameters of the Shikoku Basin clay to obtain the maximum influence of compaction of interbedded clay layers. For the LSB sandstone,

we used the deeper LSB clay parameters from Muroto samples (Hüpers et al., 2010) to obtain maximum compaction results (Table 5-1).

A coefficient of friction ( $\chi$ ) is necessary for the contact between the accretionary hanging and footwall of the frontal thrust. Ikari et al. (2007) studied the effects of hydration on frictional properties of montmorillonite-quartz fault gouge material. They found their coefficient of friction values were in agreement with Saffer and Marone (2003) values for 100% and 50% montmorillonite. Dependent on the amount of stress, water content, and clay content, Ikari et al. (2007) found a range of  $\chi$  of 0.59 (with 50% montmorillonite and 5 MPa) to 0.12 (with 100% montmorillonite and 100 MPa). We used the average,  $\chi$  of 0.3 for the base model and ran sensitivity simulations varying  $\chi$  from 0.1 to 0.35. Increasing  $\chi$  above 0.35 resulted in excessive deformation of the model region and was judged to be unrealistic.

Table 5-1. The parameters used within the base model simulations with references

Part	E	Reference	$\nu$	Reference	$\Lambda$	Corrected $\Lambda$	K	Reference
Prism	$5 \times 10^8$	-	0.3	Masterlark (2003)	-	-	-	-
Trench	-	-	0.3	Masterlark (2003)	0.117	0.3	0.014	Bellew (2004); Hüpers et al. (2010)
Shikoku Basin Clay	-	-	0.3	Masterlark (2003)	0.117	0.3	0.014	Bellew (2004); Hüpers et al. (2010)
LSB Sandstone	-	-	0.3	Masterlark (2003)	0.78	-	0.02	Bellew (2004); Hüpers et al. (2010)
Basalt	$1 \times 10^{11}$	Domenico and Schwartz (1998)	0.3	Masterlark (2003)	-	-	-	-

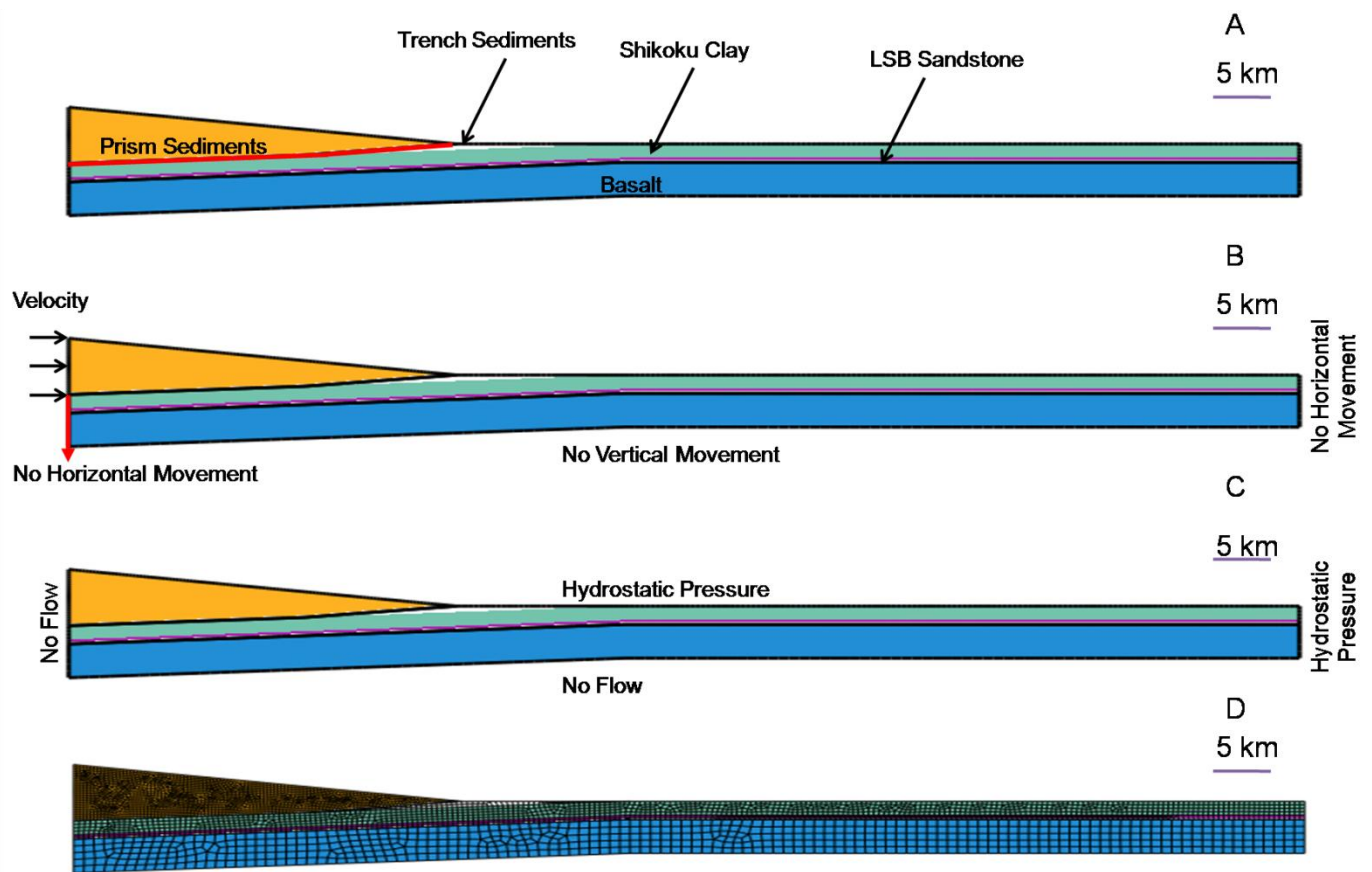


Figure 5-1. An illustration of the model setup. A) The left side represents landward and the frontal thrust fault is highlighted in red. B) The mechanical boundary conditions applied to the model. C) The hydrostatic and no flow boundary conditions for the model. D) The model after it has been meshed.

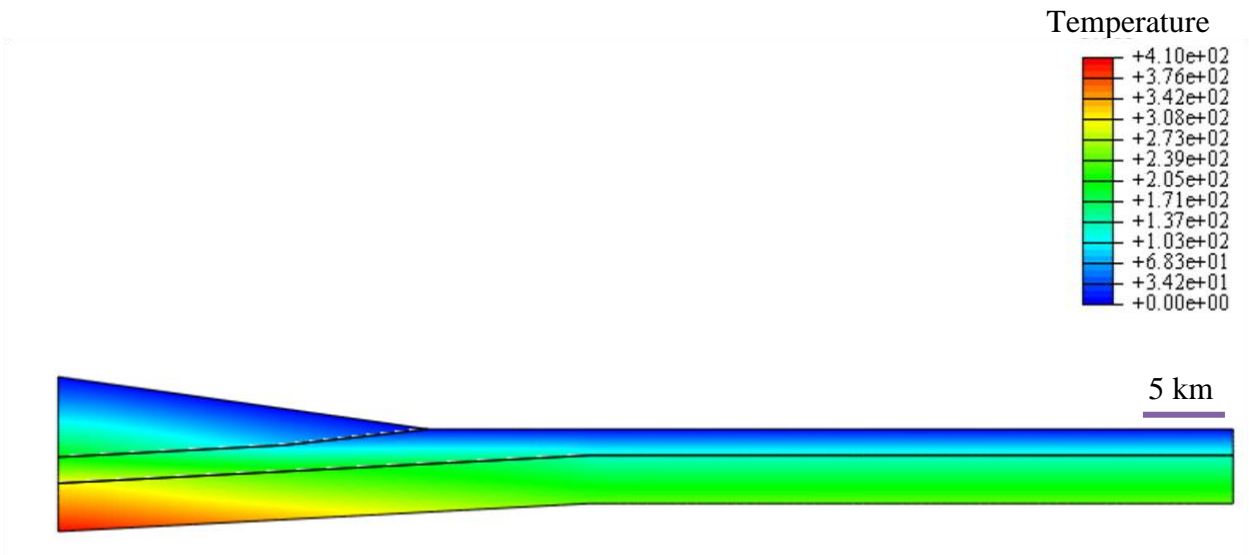


Figure 5-2. The temperature distribution used for viscosity calculations

## CHAPTER 6 RESULTS

### **Permeability Results**

Permeability tests were run on a total of nine samples from the toe region. All were from shallow depth (< 0.6 km beneath the seafloor). The porosities of Sites C0006 and C0007 samples ranged from ~0.2 to 0.4 and ~0.3 to 0.5, respectively. The measured permeabilities at Site C0006 span from  $3 \times 10^{-19}$  to  $4 \times 10^{-17} \text{ m}^2$ , and Site C0007 permeabilities ranged from  $2 \times 10^{-18}$  to  $9 \times 10^{-17} \text{ m}^2$  (Figure 6-1).

The lithology of Sites C0006 and C0007 varies with depth, ranging from sandy slope sediments to hemipelagic mud. Grain-size analysis performed by Kopf et al. (in review) allows the quantitative separation of the samples. The grouping is based on the grouping of Bryant (2002) and also used by Gamage et al. (2011). Group 1 includes sediments with greater than 80% clay size particles. Group 2 includes sediments with 60–80% clay size material. Group 3 includes the sediments with less than 60% clay-sized material and less than 5% sand. Group 4 includes the sediments that are less than 60% clay-sized material and greater than 5% sand (Gamage et al., 2011).

Three measured samples were from the Shikoku Basin clay. The permeability-porosity results of the Shikoku Basin clay samples from Kumano appear consistent with the permeability-porosity trends of the Shikoku Basin clay based on samples from the Muroto transect (Figure 6-2). The relationship of Skarbek and Saffer (2009) was used for the base model simulation.

### **Modeling Results**

Initial model runs were used to determine the appropriate Cam Clay parameters for the Shikoku Basin clay by comparing simulated porosity-depth profiles 20 km

seaward of the trench to the observed profile from Site C0011. A  $\lambda$  of 0.3 was determined to provide a reasonable match to the observed data.

### **Base Model Results**

As the hanging wall is displaced over the footwall, excess pore pressures were generated beneath the toe of the accretionary prism and migrated horizontally with the prism. A plot of excess pore pressure through time within the Shikoku Basin clay in the footwall, illustrates the gradual increase in pore pressure due to the overriding prism (Figure 6-3). Superimposed on the gradual increase, slight fluctuations with lower and higher pressure occur during the displacement of the prism (Figure 6-4). Though a constant velocity is applied to the frontal thrust slip, the coefficient of friction influences the ease of slip. With a constant coefficient of friction, variations in pore pressures can alter the effective stress and cause intermittent slip of the frontal thrust.

Looking at the final model results, which represent the present time, the base model shows that excess pore pressure forms a horizontally elliptical shape beneath the frontal thrust within the Shikoku Basin clay and above the LSB sandstone (Figure 6-4). The model results in an EPP greater than 1MPa and an excess pore pressure ratio,  $\lambda^*$ , of 0.34. The maximum pore pressures are generated landward of the trench and do not appear seaward of the trench.

Excess pore pressure and effective stress with depth profile were created at the trench and 7 km landward of the trench. At the trench, the maximum excess pore pressure occurs around ~0.75 km in depth from the top of the footwall. The effective stress at the trench continually increases with depth (Figure 6-4). At 7 km landward of the trench, the maximum EPP is located ~0.65 km below from the top of the footwall.

The stress profile reflects a minimum in effective stress ~0.6 km below the top of the footwall (Figure 6-4).

At the trench, the effective horizontal stress is greater than the effective vertical stress until 0.8 km depth (Figure 6-4). At 7km landward of the trench, the vertical effective stress is consistently larger than the effective horizontal stress. There is a localized zone of horizontal compression located near the trench. The horizontal displacement illustrates that the thrust of the prism along the frontal thrust is felt within the footwall sediments at the trench (Figure 6-5).

In general, the fluid flow in the Shikoku Basin clay beneath the thrust fault is diverted upward towards the trench sediment or downwards towards the LSB sandstone (Figure 6-6). The highest flow rates occur horizontally along the buried LSB sandstone. The maximum fluid flow velocity in the base model was  $2.3 \times 10^{-10}$  m/s within the LSB sandstone.

### **Sensitivity Results**

With permeability being a key parameter in the investigation, the prism, trench sediment, LSB sandstone, and Shikoku Clay permeabilities were altered in the sensitivity runs. To represent the multiple faults within the prism, we increased the permeability of the prism sediments. Increasing permeability within the prism had very minor effect on the pore pressure ratio and fluid flow within the footwall.

To test sensitivity to the permeability of the LSB sandstone, we decreased the permeability an order of a magnitude. This resulted in a  $\lambda^*$  of 0.38 (Figure 6-7). The velocity along the LSB sandstone decreased to  $1.5 \times 10^{-10}$  m/s from the base model ( $2.3 \times 10^{-10}$  m/s) (Table 6-1). In a separate run, the permeability of the trench sediments was decreased by an order of magnitude. The simulation yielded  $\lambda^*=0.56$  (Figure 6-7) and

the fluid velocity within the LSB sandstone increased to  $2.7 \times 10^{-10}$  m/s. The EPP pattern in both models was very similar to the base model, with the highest EPP within the Shikoku Basin clay, about ~7 km seaward of the trench and about ~0.6 km in depth from the top of the footwall.

The sensitivity to the Shikoku Basin clay permeability-porosity relationship was examined by using the relationship found by Gamage and Screaton (2006) rather than that of Skarbek and Saffer (2009) used in the base model. The resulting excess pore pressure ratio,  $\lambda^*$  was 0.19, which is significantly lower than the base run ( $\lambda^*=0.34$ ) (Figure 6-7). The maximum pore pressure location was similar to the base model, as well as the fluid flow pattern. The maximum fluid flow rate,  $2.3 \times 10^{-10}$  m/s, appeared in the LSB sandstone (Table 6-1).

We compared the Cam Clay,  $\Lambda$ , of 0.3 that best matched the Site C0011 porosities from the Kumano Basin transect to  $\Lambda$  derived from samples from the Muroto transect tested by Bellew (2004) that yielded a  $\Lambda=0.117$ . Decreasing the compaction parameter resulted in a significant reduction of  $\lambda^*$  to 0.005 (Figure 6-7). The velocity of the fluid flow within the LSB sandstone is decreased to  $6.9 \times 10^{-11}$  m/s (Table 6-1). The pattern of EPP and fluid flow are similar to the base model results.

With a higher coefficient of friction (0.35) applied to the frontal thrust, the pore pressure increased from the base model run, yielding a maximum  $\lambda^*$  of 0.40 (Figure 6-7). With a lower coefficient of friction (0.1), a decrease in pore pressure occurred, with a maximum  $\lambda^*$  of 0.20 (Figure 6-7). The fluid patterns are similar to the base model yielding a maximum fluid velocity within the LSB sandstone of  $2.5 \times 10^{-10}$  m/s and  $1.9 \times 10^{-10}$  m/s, for a 0.35 and 0.1 coefficient of friction run, respectively (Table 6-1).

Altering the fault slip rate generated varying excess pore pressure ratios.

Decreasing the amount of time to 0.436 My, the lower end of the range given by Screatton et al (2009a) resulted in a  $\lambda^*$  of 0.40, while increasing the time to 0.78 My resulted in a lower  $\lambda^*$  of 0.29 (Figure 6-7). The velocity of fluid flow within the LSB sandstone was  $2.9 \times 10^{-10}$  m/s and  $1.8 \times 10^{-10}$  m/s for the slip time of 0.436 My and 0.78 My, respectively (Table 6-1). The EPP locations and the fluid flow patterns are similar to the results of the base model.

Table 6-1. Maximum simulated excess pore pressures (Pa), the calculated  $\lambda^*$ , and the maximum fluid velocity (m/s).

Run	EPP (Pa)	$\lambda^*$	Velocity (m/s)
Base	8.37E+06	0.37	2.26E-10
Decrease Slip Rate	6.72E+06	0.30	1.79E-10
Increase Slip Rate	1.02E+07	0.44	2.93E-10
Decrease k in Trench	1.14E+07	0.56	2.74E-10
Decrease k in LSB sandstone	8.42E+06	0.38	1.50E-10
Gamage and Screatton (2006) k	3.98E+06	0.19	2.72E-10
High Coefficient of Friction	9.82E+06	0.39	2.48E-10
Low Coefficient of Friction	5.67E+06	0.23	1.90E-10
Cam Clay	7.71E+04	0.00	6.87E-11

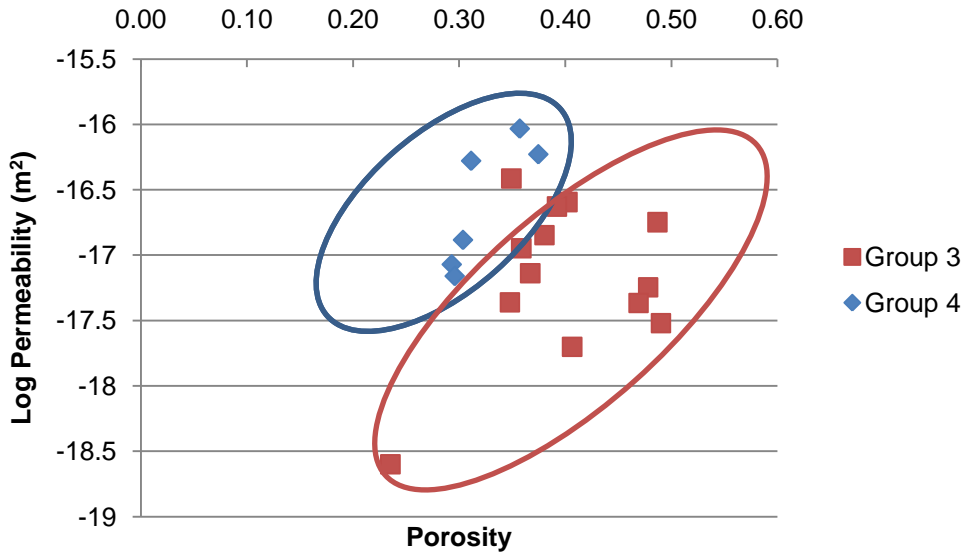


Figure 6-1. The grain-size grouping of the permeability of Sites C0006 and C0007 samples plotted as a function of porosity. Samples are grouped by the grain-size classification of Bryant et al. (2002).

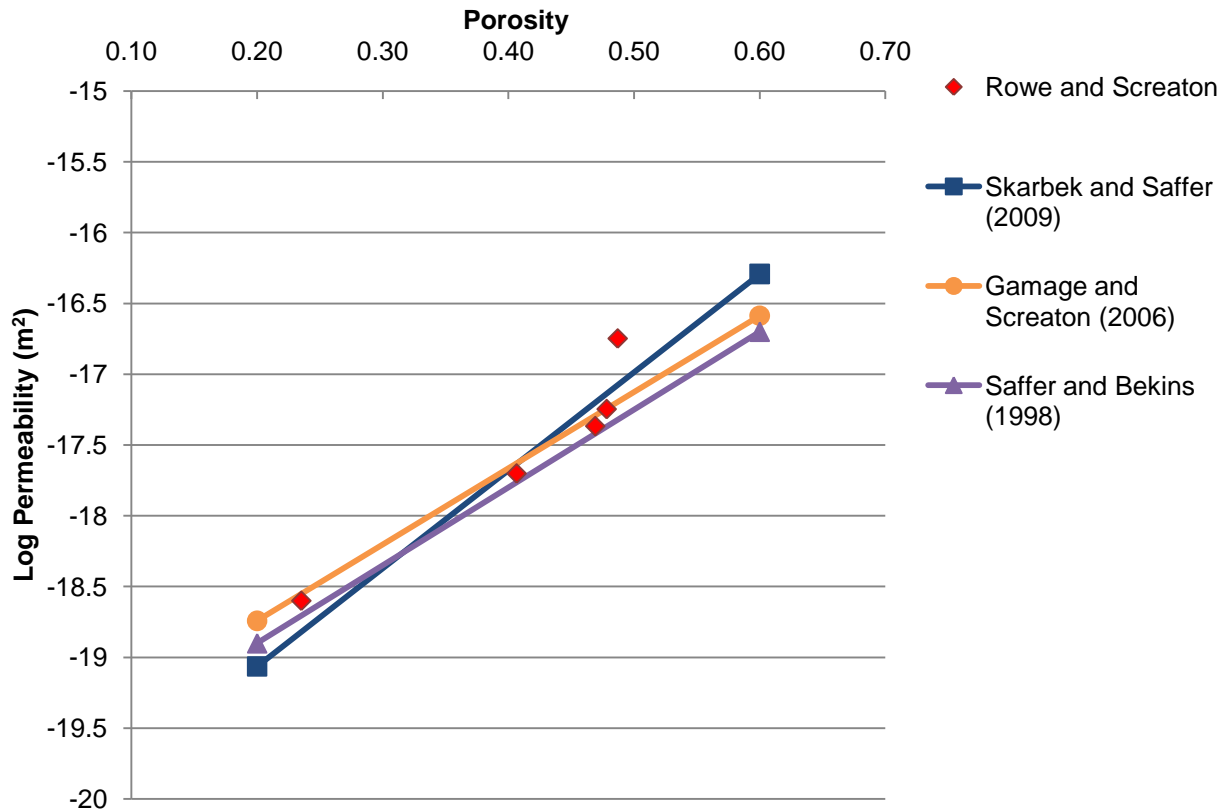


Figure 6-2. The Shikoku Basin facies permeability-porosity trends from the Muroto transect and the Shikoku Basin clay results from the Kumano Basin transect (in red).

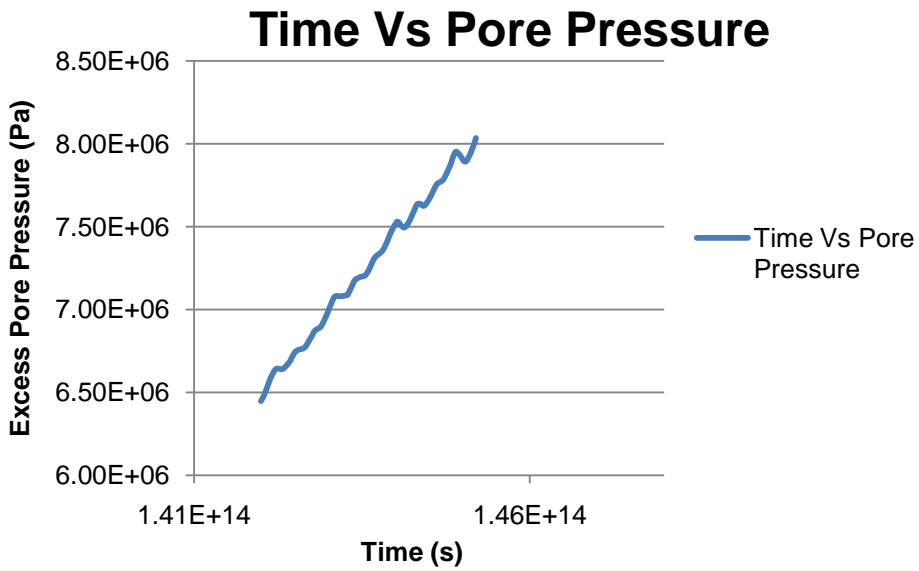


Figure 6-3. Simulated excess pore pressure through time.

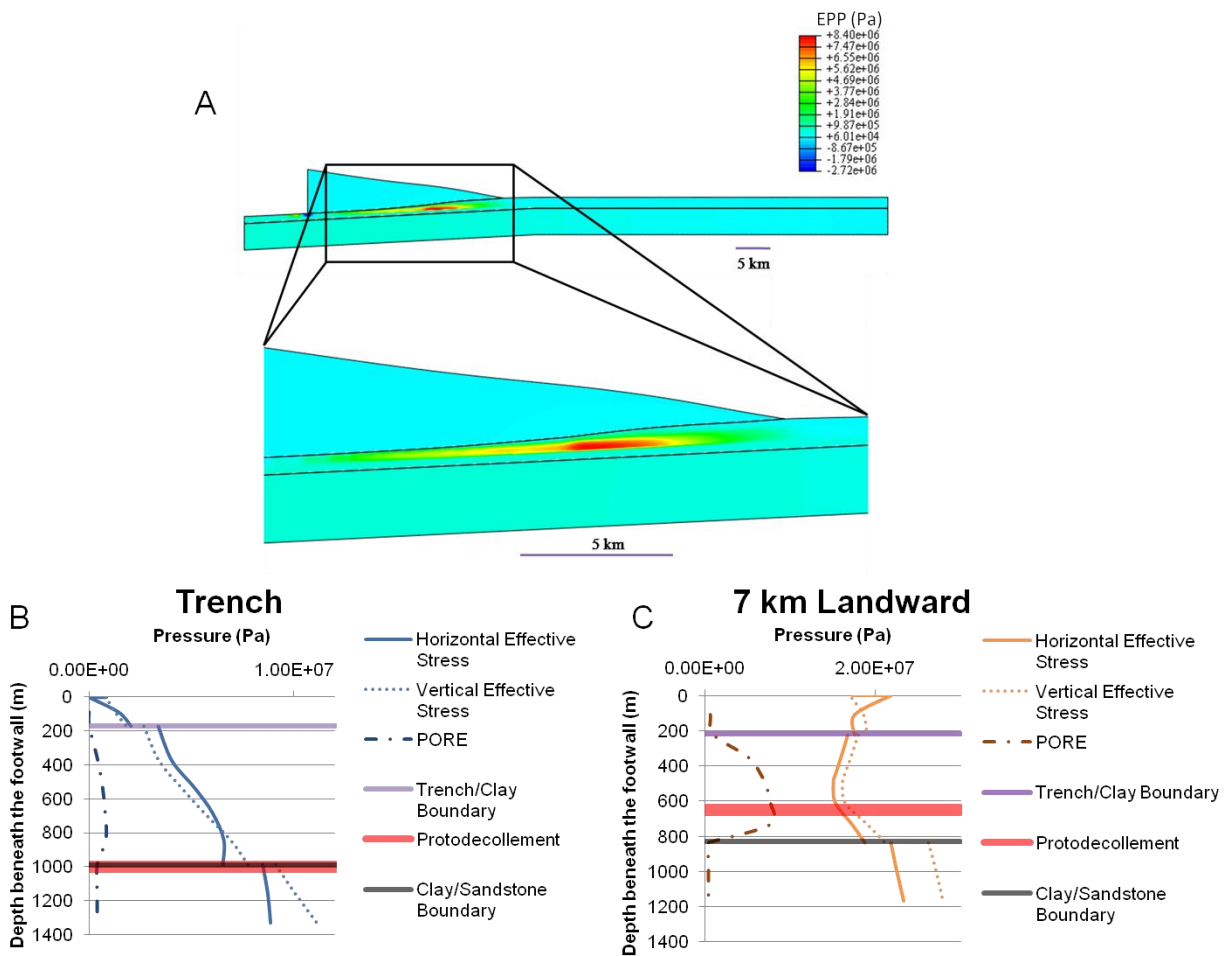


Figure 6-4. The excess pore pressure results. A) The excess pore pressure results of the base model. B) The trench profile of the excess pore pressures (noted as PORE) at depth in both the base and maximum model. The top depth represents the top of the footwall. C) The effective stresses and excess pore pressures occur 7 km landward of the trench.

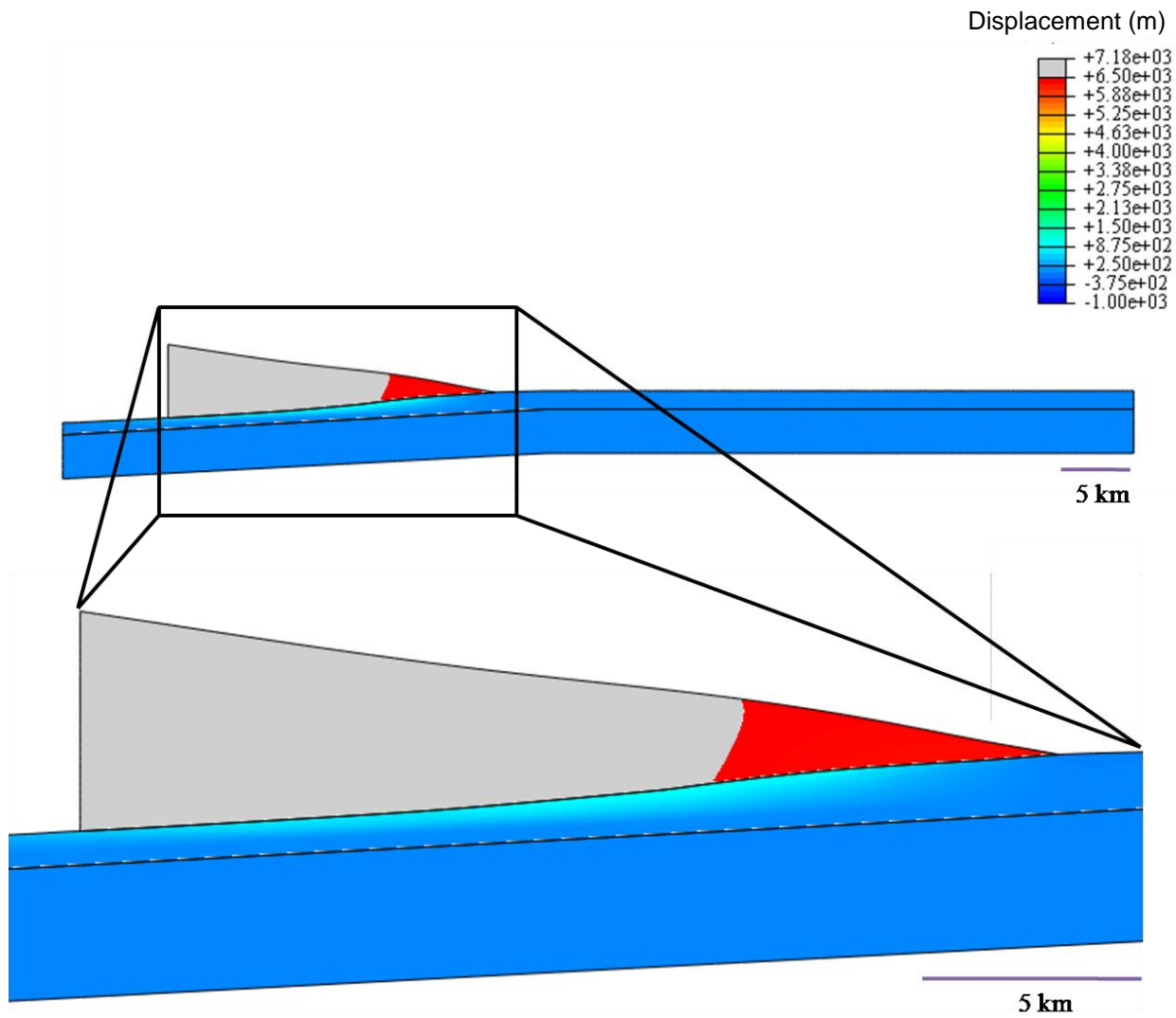


Figure 6-5. Cumulative horizontal displacement simulated with the base model.

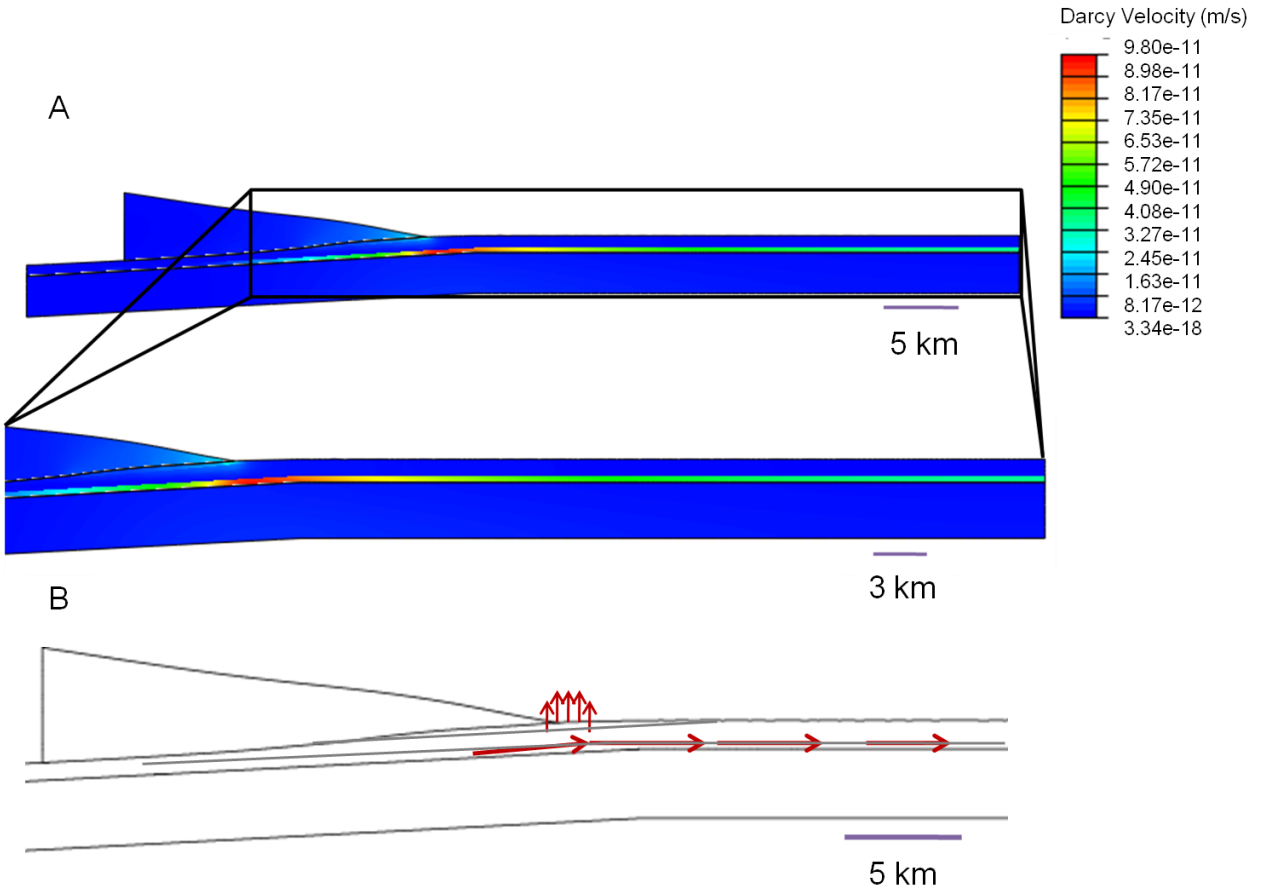


Figure 6-6. The fluid flow results. A) The Darcy's velocity magnitude (velocity\*porosity) of the base model. B) A schematic illustrating flow direction in the trench sediments and LSB sandstone.

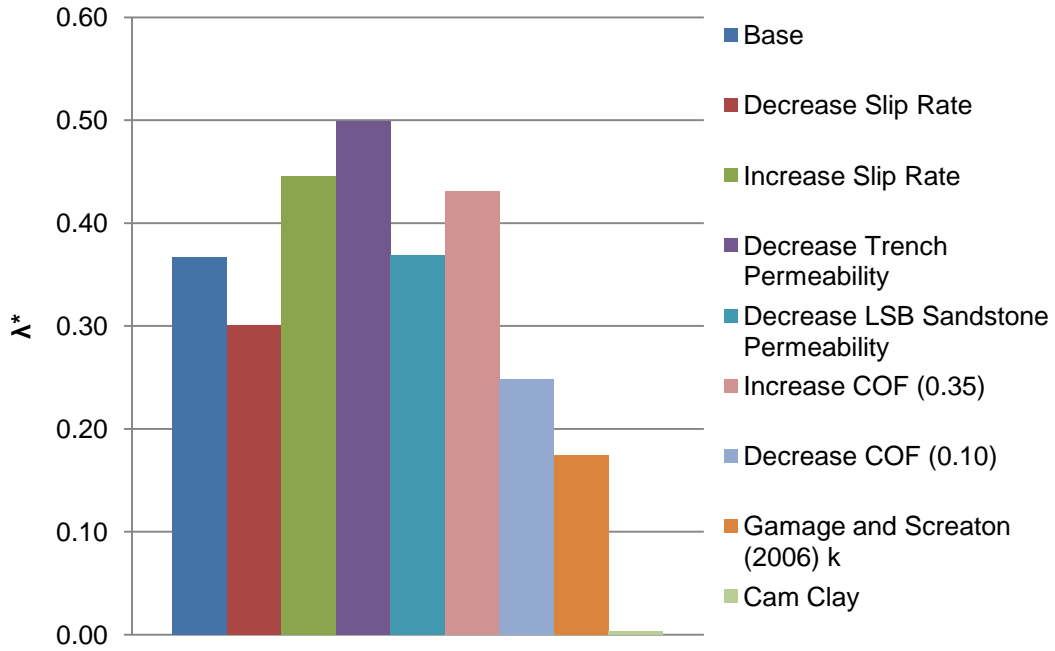


Figure 6-7. The excess pore pressure ratio results for the sensitivity analyses. The base model is the blue column on the far left.

## CHAPTER 7 DISCUSSION

### **Pore Pressure and Fluid Flow**

Overall, the model simulated high excess pore pressures within the Shikoku Basin clay. Sensitivity runs confirmed the high pore pressure generation except for the simulation using the Gamage and Scretton (2006) porosity-permeability relationship and the simulation with a Cam Clay parameter,  $\lambda$ , of 0.117. The excess pore pressures reach a maximum beneath the frontal thrust ~7 km landward of the trench, but significant excess pore pressures do not extend seaward of the trench. The simulated excess pore pressure ratios of the base model are not as high as that estimated for the Muroto transect (Scretton et al., 2001; Saffer, 2003), likely due to fluid escape along the LSB sandstones, which do not occur in the Muroto transect.

The model results are very sensitive to the permeability-porosity relationship and consolidation parameters of the Shikoku Basin clay. The Shikoku Basin clay samples tested in this study exhibit a very similar permeability-porosity trend to the previous relationships of the Muroto transect (Figure 6-2) despite very different temperature condition along the Muroto and Kumano Basin transects. This similarity supports the general results of Gamage et al. (2011), who found that the permeability-porosity trends of shallow sediments are less dependent on temperature or region than on the grain size within the samples. However, the seemingly small change in the relationships between the Skarbek and Saffer (2009) and the Gamage and Scretton (2006) drops the excess pore pressure ratio from  $\lambda^*=0.37$  to 0.19. The limited number of Shikoku Basin clay samples tested leaves room to suggest that either permeability-porosity

relationship could be applied. Additional results will become available from laboratory tests on samples from Expedition 322 and 333 and may help refine the model results.

The Cam Clay  $\Lambda$  parameter also has a significant effect on the location and magnitude of excess pore pressure production. The model with the low  $\Lambda$  resulted in minimal excess pore pressures,  $\lambda^*=0.005$ , within the Shikoku Basin clay, ~3 km landward of the trench, and at a deeper depth, ~900 m from the top of the footwall. Although this simulation is useful for understanding the role of compaction, the  $\Lambda$  value is considered unrealistically low because it results in simulated porosities higher than measured at Site C0011.

Because of their high permeability relative to the Shikoku Basin clays, the LSB sandstone and trench sediments are zones of high flow velocity. At their highest, the velocities of the fluid flow within LSB sandstone are in the same order of magnitude of the frontal thrust slip rate. As the fluid flows seaward, the velocity decreases by an order of magnitude >20 km from the trench. This fluid velocity within our model is not consistent with the freshening and potentially deeper regional chemical signals observed at Site C0011 that suggest that fluid has traveled through the sand rich units from deeper within the subduction zone. For geochemical signals to reach Site C0011, the fluid velocity must have exceeded the movement of the prism toe.

One reason that the simulated flow rates are underestimates could be the assumption of a steady frontal thrust slip rate. Larger, but short-lived, slip could cause transient bursts of fluid flow or small units of high permeability. Saffer and Bekins (1998) illustrated a similar idea by simulating a sudden increase in fault zone permeability allowing the fluid to escape to achieve the velocity and flow of a chemical signal.

Another reason for lower simulated velocities could be the exclusion of fluid migrating from landward of our model boundary, due to our model focusing on shallow processes. If the sand units remain an open conduit with greater depth, the water may be escaping with an increased velocity that is not modeled.

### **Décollement Propagation**

The PTZ observations from the seismic reflection data locate the protodécollement ~1 km below the seafloor at the trench (Moore et al., 2009) (Figure 2-3). Le Pichon and Henry (1992) suggest that the protodécollement location is controlled by a maximum excess pore pressure and a minimum in effective stress caused by rapid loading whereas Raimbourg et al. (2011) suggest that the location is controlled by horizontal stress created by movement of the prism. At 7km landward of the trench, the excess pore pressure profile illustrates a maximum in EPP and an effective stress minimum ~0.6 km from the top of the footwall. These results coincide with the inferred PTZ location (Figure 2-3) and thus support Le Pichon and Henry's (1992) hypothesis for décollement propagation. Looking at the effective horizontal and vertical stresses at this location, we can see the vertical stress is consistently greater than the horizontal stress with depth. There is no rotation of stress or suggestions of horizontal stress formation of the protodécollement as suggested by Raimbourg et al., 2001 (Figure 6-5).

Results are significantly different at the trench, where the excess pore pressure is small. There is an increase in excess pore pressure around ~0.8km of depth from the top of the footwall, which is consistent with the PTZ location (Figure 2-3). However, the effective stress continuously increases with depth, which disagrees with the mechanism for initiation of the protodécollement suggested by Le Pichon and Henry (1992). It is possible that the loading by trench sediment deposition, which is not simulated in our

model, could increase pore pressures and decrease effective stress. Our model results show a stress rotation below the trench. From 0–0.7 km of depth from the top of the footwall, the horizontal stress is greater than the vertical stress, while below 0.8 km the vertical stress is greater than the horizontal (Figure 6-5). From our model, the zone (0.7 and 0.8 km depth from footwall) of horizontal and vertical stress transition appears consistent with potential décollement formation. The horizontal and vertical stress profile illustrates the potential for the protodécollement localization due to horizontal stress mechanism suggested by Raimbourg et al. (2011).

The mechanisms of protodécollement initiation by Le Pichon and Henry (1992) were observed landward of the trench, while the mechanisms by Raimbourg et al. (2011) were observed at the trench. The modeling results suggest both mechanisms contribute to creating and propagating the protodécollement.

## CHAPTER 8 CONCLUSIONS

Our modeling results suggest that the Kumano Basin transect could contain significant excess pore pressures, with a simulated  $\lambda^*$  of 0.37, located 7 km landward of the trench beneath the frontal thrust ~0.7 km in depth from the top of the footwall and within the Shikoku Basin clay. The resulting excess pore pressures are small at the trench and continually decrease seaward of the trench.

The flow patterns of the simulations illustrate horizontal flow within the LSB sandstone and vertical flow in the trench sediments. Our fluid flow velocity is consistently less than the thrust fault slip, contrary to geochemical observations. Geochemical signals could require rapid but short-lived thrust movements that can generate a pulse of fluid velocity or additional flow from greater depths than simulated in our model.

At 7 km landward of the trench, the protodécollement propagation is dependent on the depth of maximum excess pore pressures and a minimum effective stress as discussed by Le Pichon and Henry (1992). At the trench, location of the protodécollement is dependent on the effective horizontal stresses that are created from the prism displacement, as discussed in Raimbourg et al. (2011). The model results illustrate both proposed mechanisms for protodécollement propagation, which suggests both could contribute to the formation and propagation of the protodécollement.

## LIST OF REFERENCES

- Abaqus 6.7 (2007), Abaqus/CAE user's manual. Dassault Systèmes Simulia Corp.
- Ando, M. (1975), Source mechanisms and tectonic significance of historical earthquakes along the Nankai Trough, Japan, *Tectonophysics*, 27, 119-140.
- Becker, K. and E. E. Davis (2004), In situ determinations of the permeability of the igneous oceanic crust, in *Hydrogeology of the Oceanic Lithosphere*, edited by E. E. Davis and H. Elderfield, pp. 189-224, Cambridge Univ. Press, United Kingdom.
- Bekins, B. A., A. M. McCaffrey, and S. J. Dreiss (1995), Episodic and constant flow models for the origin of low-chloride waters in a modern accretionary complex, *Water Resour. Res.*, 31(12), 3205-3215.
- Bellew, G. (2004), Consolidation properties, stress history, and modeling pore pressures for deep sea sediments at the Nankai Trough, M. S. thesis, University of Missouri-Columbia.
- Bryant, W. (2002), Permeability of clays, silty-clays and clayey-silts, *Transactions - Gulf Coast Association of Geological Societies*, 52, 1069-1077.
- Christensen, N. I. (1996), Poisson's ratio and crustal seismology, *Journal of geophysical research*, 101(b2), 3139-3156.
- Davis, E. E. and K. Becker (2002), Observations of natural-state fluid pressures and temperatures in young oceanic crust and inferences regarding hydrothermal circulation, *Earth Planet. Sci. Lett.*, 204(1-2), 231-248, doi: 10.1016/S0012-821X(02)00982-2.
- Davis, E. E., K. Wang, K. Becker, and R. E. Thomson (2000), Formation-scale hydraulic and mechanical properties of oceanic crust inferred from pore pressure response to periodic seafloor loading, *Journal of geophysical research*, 105(b6), 13423-13.
- Domenico, P. A. and F. W. Schwartz (1998), *Physical and Chemical Hydrogeology*, 2nd Edition ed., John Wiley & Sons Inc., New York.
- Expedition 314 Scientists (2009), Expedition 314 Site C0006. In Kinoshita, M., H. Tobin, J. Ashi, G. Kimura, S. Lallemant, E. J. Screaton, D. Curewitz, D., H. Masago, K. T. Moe, and the Expedition 314/315/316 Scientists, *Proc. IODP, 314/315/316: Washington, DC (Integrated Ocean Drilling Program Management International, Inc.)*, doi:10.2204/iodp.proc.314315316.118.2009

- Expedition 316 Scientists (2009a), Expedition 316 Site C0006. In Kinoshita, M., H. Tobin, J. Ashi, G. Kimura, S. Lallemand, E. J. Screaton, D. Curewitz, H. Masago, K. T. Moe, and the Expedition 314/315/316 Scientists, Proc. IODP, 314/315/316: Washington, DC (Integrated Ocean Drilling Program Management International, Inc.), doi:10.2204/iodp.proc.314315316.134.2009
- Expedition 316 Scientists (2009b), Expedition 316 Site C0007. In Kinoshita, M., H. Tobin, J. Ashi, G. Kimura, S. Lallemand, E. J. Screaton, D. Curewitz, H. Masago, K. T. Moe, and the Expedition 314/315/316 Scientists, Proc. IODP, 314/315/316: Washington, DC (Integrated Ocean Drilling Program Management International, Inc.), doi:10.2204/iodp.proc.314315316.135.2009
- Fisher, A. T. (2005), Marine hydrogeology: recent accomplishments and future opportunities, *Hydrogeology Journal*, 13.
- Gamage, K., and E. Screaton (2003), Data report: Permeabilities of Nankai accretionary prism sediments. In Mikada, H., Moore, G.F., Taira, A., Becker, K., Moore, J.C., and Klaus, A. (Eds.), Proc. ODP, Sci. Results, 190/196, 1–22 [Online]. Available from World Wide Web: <<http://www-dp.tamu.edu/publications/190196SR/VOLUME/CHAPTERS/213.PDF>>.
- Gamage, K. and E. Screaton (2006), Characterization of excess pore pressures at the toe of the Nankai accretionary complex, Ocean Drilling Program Sites 1173, 1174, and 808; results of one-dimensional modeling, *Journal of geophysical research*, 111(b4), doi: 10.1029/2004JB003572.
- Gamage, K., E. Screaton, B. Bekins, and I. Aiello (2011), Permeability–porosity relationships of subduction zone sediments, *Mar. Geol.*, 279(1-4), 19-36, doi: DOI: 10.1016/j.margeo.2010.10.010.
- Helwany, S. (2007), *Applied Soil Mechanics : With ABAQUS Applications*, John Wiley & Sons.
- Hughes, K. L. H., T. Masterlark, and W. D. Mooney (2010), Poroelastic stress-triggering of the 2005 M8.7 Nias earthquake by the 2004 M9.2 Sumatra–Andaman earthquake, *Earth Planet. Sci. Lett.*, 293(3-4), 289-299, doi: DOI: 10.1016/j.epsl.2010.02.043.
- Hüpers, A., S. Kreiter, and A. J. Kopf (2010), Ramifications of high in-situ temperatures for laboratory testing and inferred stress states of unlithified sediments – A case study from the Nankai margin, *Mar. Pet. Geol.*, 27(7), 1565-1571, doi: DOI: 10.1016/j.marpetgeo.2010.03.014.
- Hüpers, A. (in prep.): Data Report: Permeabilities and consolidation properties of sandy sediments from the Nankai Trough, IODP Sites C0011 and C0012, Proceeding of the Integrated Ocean Drilling Program

- Ikari, M. J., D. M. Saffer, and C. Marone (2007), Effect of hydration state on the frictional properties of montmorillonite-based fault gouge, *Journal of geophysical research*, 112(b6), B06423.
- Ike, T., G. F. Moore, S. Kuramoto, J. Park, Y. Kaneda, and A. Taira (2008), Variations in sediment thickness and type along the northern Philippine Sea Plate at the Nankai Trough, Island Arc, 17(3), 342-357, doi: 10.1111/j.1440-1738.2008.00624.x.
- Ingebritsen, S. (2006), *Groundwater in Geologic Processes*, 2nd Edition ed., Cambridge University Press, Cambridge.
- King, G. C. P., R. S. Stein, and J. Lin (1994), Static stress changes and the triggering of earthquakes, *Bulletin of the Seismological Society of America*, 84(3), 935-953.
- Kinoshita, M., T. Kanamatsu, K. Kawamura, T. Shibata, H. Hamamoto, and K. Fujino (2008), Heat flow distribution on the floor of Nankai Trough off Kumano and implications for the geothermal regime of subducting sediments, *JAMSTEC report of research and development*, 8, 13-28.
- Kopf, A. J., M. Strasser, N. Monsees, M.B. Underwood, and J. Guo (in press), Data Report: Particle size analysis of sediments recovered during IODP Expedition 315 and 316, Sites C0001–C00008, Nankai Trough forearc, off Japan, *Proceedings of the integrated Ocean Drilling Program*
- Kummer, T. and G. A. Spinelli (2009), Thermal effects of fluid circulation in the basement aquifer of subducting ocean crust, *Journal of geophysical research*, 114(b3), B03104, doi: doi: 10.1029/2008JB006197.
- Le Pichon, X. and P. Henry (1992), Erosion and accretion along subduction zones: a model of evolution, *Eos (Washington, D.C.)*, 73(14), 294.
- Masterlark, T. (2003), Finite element model predictions of static deformation from dislocation sources in a subduction zone: Sensitivities to homogeneous, isotropic, Poisson-solid, and half-space assumptions, *Journal of geophysical research*, 108(b11).
- Masterlark, T. and K. L. Hughes (2008), Next generation of deformation models for the 2004 M9 Sumatra-Andaman earthquake, *Geophys. Res. Lett.*, 35(19), L19310.
- Masterlark, T. and H. F. Wang (2000), Poroelastic coupling between the 1992 Landers and Big Bear Earthquakes, *Geophys. Res. Lett.*, 27(22), 3647-3650.

- Miyazaki, S. and K. Heki (2001), Crustal velocity field of southwest Japan: Subduction and arc-arc collision, *Journal of geophysical research*, 106(b3), 4305-4326.
- Moore, G.F., H. Mikada, J.C. Moore, K. Becker, and A. Taira (2005), Legs 190 and 196 synthesis: deformation and fluid flow processes in the Nankai Trough accretionary prism. In Mikada, H., G. F. Moore, A. Taira, K. Becker, J.C. Moore, A. Klaus (Eds.), *Proc.ODP, Sci. Results*, 190/196, 1–26 [Online]. Available from World Wide Web: <http://www-odp.tamu.edu/publications/190196SR/VOLUME/SYNTH/SYNTH.PDF>
- Moore, G. F., J.-O. Park, N.L. Bangs, S.P. Gulick, H.J. Tobin, Y. Nakamura, S. Sato, T. Tsuji, T. Yoro, H. Tanaka, S. Uraki, Y. Kido, Y. Sanada, S. Kuramoto, A. Taira (2009), Structural and seismic stratigraphic framework of the NanTroSEIZE Stage 1 transect. In Kinoshita, M., H. Tobin, J. Ashi, G. Kimura, S. Lallement, E.J. Screaton, D. Curewitz, H. Masago, K.T. Moe, the Expedition 314/315/316 Scientists, *Proc. IODP, 314/315/316: Washington, DC (Integrated Ocean Drilling Program Management International, Inc.)*. doi:10.2204/iodp.proc.314315316.102.2009
- Moore, G. F., A. Taira, A. Klaus, L. Becker, B. Boecker, B. A. Cragg, A. Dean, C. L. Fergusson, P. Henry, S. Hirano, T. Hisamitsu, S. Hunze, M. Kastner, A. J. Maltman, J. K. Morgan, Y. Murakami, D. M. Saffer, M. Sa´nchez-Gómez, E. J. Screaton, D. C. Smith, A. J. Spivack, J. Steurer, H. J. Tobin, K. Ujiie, M. B. Underwood, and M. Wilson (2001), New insights into deformation and fluid flow processes in the Nankai Trough accretionary prism: Results of Ocean Drilling Program Leg 190, *Geochem. Geophys. Geosyst.*, 2, 10.129/2001GC000166, 2001.
- Moore, J. C. (1989), Tectonics and hydrogeology of accretionary prisms: role of the décollement zone, *J. Struct. Geol.*, 11(1-2), 95-106.
- Raimbourg, Hugues, K.Ujiie, A. Kopf., T. Hisamitsu, Y. Hamano, S. Saito, and M. Kinoshita (2011), The role of compaction contrasts in sediments in décollement initiation in an accretionary prism, *Marine Geology*, doi:10.1016/j.margeo.2011.02.011
- Roscoe, K.H., and J.B. Burland (1968), On the generalised stress–strain behaviour of wet clay. In *Engineering plasticity*, Edited by J. Heyman and F.P. Leckie. Cambridge University Press, New York
- Rowe, K., E. Screaton, J. Guo, and M. B. Underwood (in review), Data Report: Permeabilities of sediments from the Kumano Basin transect offshore the Kii Peninsula, Japan, *Proceedings of the integrated Ocean Drilling Program*
- Ruff, L. and H. Kanamori (1983), Seismic coupling and uncoupling at subduction zones, *Tectonophysics*, 99(2-4), 99-117.

- Saffer, D. (2003), Pore pressure development and progressive dewatering in underthrust sediments at the Costa Rican subduction margin: Comparison with northern Barbados and Nankai, *Journal of geophysical research*, 108(b5), 2261.
- Saffer, D. M. (2007), Pore pressure within underthrust sediment in subduction zones, In Dixon, T. H. and J. C. Moore (eds.), *The seismogenic zone of subduction thrust faults*, Columbia University Press, New York, 171-205
- Saffer, D. (2010), Hydrostratigraphy as a control on subduction zone mechanics through its effects on drainage: an example from the Nankai Margin, SW Japan, *Geofluids*, 10(1-2), 114-131, doi: 10.1111/j.1468-8123.2009.00276.x.
- Saffer, D. and B. A. Bekins (1998), Episodic fluid flow in the Nankai accretionary complex: Timescale, geochemistry, flow rates, and fluid budget, *Journal of geophysical research*, 103(b12), 30351-30370.
- Saffer, D. M. and B. A. Bekins (2002), Hydrologic controls on the morphology and mechanics of accretionary wedges, *Geology (Boulder)*, 30(3), 271-274.
- Saffer, D. M. and B. A. Bekins (2006), An evaluation of factors influencing pore pressure in accretionary complexes: Implications for taper angle and wedge mechanics, *Journal of geophysical research*, 111(b4), B04101.
- Saffer, D. M. and C. Marone (2003), Comparison of smectite- and illite-rich gouge frictional properties: application to the updip limit of the seismogenic zone along subduction megathrusts, *Earth Planet. Sci. Lett.*, 215(1-2), 219-235, doi: DOI: 10.1016/S0012-821X(03)00424-2.
- Schofield, A., and P. Wroth (1968), *Critical state soil mechanics*, McGraw Hill, London
- Schwartz, F. W., and H. Zhang (2003), *Fundamentals of groundwater*, Wiley, New York
- Screaton, E. (2010), Recent advances in subseafloor hydrogeology: focus on basement–sediment interactions, subduction zones, and continental slopes, *Hydrogeology Journal*, 18, 1547-1570.
- Screaton, E., G. Kimura, D. Curewitz, and et al. (2009), Interactions between deformation and fluids in the frontal thrust region of the NanTroSEIZE transect offshore the Kii Peninsula, Japan: Results from IODP Expedition 316 Sites C0006 and C0007, *Geochemistry, geophysics, geosystems* : G3, 10, Q0AD01, doi: 10.1029/2009GC002713.

- Screaton, E., D. Saffer, P. Henry, S. Hunze, and Leg 190 Shipboard Scientific Party (2002), Porosity loss within the underthrust sediments of the Nankai accretionary complex: Implications for overpressures, *Geology* (Boulder), 30(1), 19-22.
- Seno, T., S. Stein, and A. E. Gripp (1993), A model for the motion of the Philippine Sea plate consistent with nuvel-1 and geological data, *Journal of geophysical research*, 98(b10), 17941-17948.
- Shipboard Scientific Party (2000), Leg 190 Preliminary Report: Deformation and fluid flow processes in the Nankai Trough accretionary prism. ODP Prelim. Rpt., 190 [Online]. Available from World Wide Web: <[http://www-odp.tamu.edu/publications/prelim/190\\_prel/190PREL.PDF](http://www-odp.tamu.edu/publications/prelim/190_prel/190PREL.PDF)>.
- Shipboard Scientific Party (2001), Leg 190 summary. In Moore, G.F., Taira, A., Klaus, A., et al., Proc. ODP, Init. Repts., 190: College Station TX (Ocean Drilling Program), 1–87.
- Skarbek, R. M. and D. M. Saffer (2009), Pore pressure development beneath the décollement at the Nankai subduction zone: Implications for plate boundary fault strength and sediment dewatering, *Journal of geophysical research*, 114(b7), B07401.
- Spinelli, G. A., P. S. Mozley, H. J. Tobin, M. B. Underwood, N. W. Hoffman, and G. M. Bellew (2007), Diagenesis, sediment strength, and pore collapse in sediment approaching the Nankai Trough subduction zone, *Geological Society of America bulletin*, 119(3-4), 377-390.
- Stauffer, P. and B. A. Bekins (2001), Modeling consolidation and dewatering near the toe of the northern Barbados accretionary complex, *Journal of geophysical research*, 106(b4), 6369-6383.
- Tobin, H.J., and M. Kinoshita (2006a), Investigations of seismogenesis at the Nankai Trough, Japan, IODP Sci. Prosp., NanTroSEIZE Stage 1, doi:10.2204/iodp.sp.nantroseize1.2006
- Tobin, H.J., and M. Kinoshita (2006b), NanTroSEIZE: the IODP Nankai Trough Seismogenic Zone Experiment. *Sci. Drill.*, 2:23–27, doi:10.2204/iodp.sd.2.06.2006
- Tobin, H. J. and D. M. Saffer (2009), Elevated fluid pressure and extreme mechanical weakness of a plate boundary thrust, Nankai Trough subduction zone, *Geology* (Boulder), 37(8), 679-682.
- Turcotte, D. L., and G. J. Schubert (1982), *Geodynamics: Applications of Continuum Physics to Geological Problems*, 450 pp., John Wiley, Hoboken, N. J.

Underwood, M.B., Saito, S., Kubo, Y., and the Expedition 322 Scientists (2009), NanTroSEIZE Stage 2: subduction inputs. IODP Prel. Rept., 322, doi:10.2204/iodp.pr.322.2009

Voss, C. I. and A. M. Provost, (2010), SUTRA: A model for saturated-unsaturated, variable-density ground-water flow with solute or energy transport, USGS, <http://water.usgs.gov/nrp/gwsoftware>

Wang, H. F. (2000), Theory of linear poroelasticity with applications to geomechanics and hydrogeology, Princeton University Press, New Jersey

## BIOGRAPHICAL SKETCH

Katherine Rowe was born in Augusta, Georgia. She attended New Smyrna Beach High School in New Smyrna Beach, Florida. She attended the University of Florida and graduated with a Bachelor of Science in geology in 2008. She received her Masters of Science degree in geology from the University of Florida in the summer of 2011.